Article

Localization atomic force microscopy

https://doi.org/10.1038/s41586-021-03551-x

Received: 20 December 2019

Accepted: 13 April 2021

Published online: 16 June 2021

Check for updates

George R. Heath[1,4], Ekaterina Kots[2], Janice L. Robertson[3], Shifra Lansky[1], George Khelashvili[2], Harel Weinstein[2] & Simon Scheuring[1,2]✉

Understanding structural dynamics of biomolecules at the single-molecule level is vital to advancing our knowledge of molecular mechanisms. Currently, there are few techniques that can capture dynamics at the sub-nanometre scale and in physiologically relevant conditions. Atomic force microscopy (AFM)[1] has the advantage of analysing unlabelled single molecules in physiological buffer and at ambient temperature and pressure, but its resolution limits the assessment of conformational details of biomolecules[2]. Here we present localization AFM (LAFM), a technique developed to overcome current resolution limitations. By applying localization image reconstruction algorithms[3] to peak positions in high-speed AFM and conventional AFM data, we increase the resolution beyond the limits set by the tip radius, and resolve single amino acid residues on soft protein surfaces in native and dynamic conditions. LAFM enables the calculation of high-resolution maps from either images of many molecules or many images of a single molecule acquired over time, facilitating single-molecule structural analysis. LAFM is a post-acquisition image reconstruction method that can be applied to any biomolecular AFM dataset.

Observing the native structure and behaviour of biomolecules is challenging owing to their architectural complexity and dynamic nature. Additionally, biomolecules can adopt multiple interchanging conformational states. Protein structure determination is progressing rapidly thanks to recent advances in cryo electron microscopy (cryo-EM) and X-ray crystallography. However, these structures represent static snapshots of averaged ensembles acquired from molecules incorporated into crystals and/or imaged at cryogenic temperature, whereas individual molecules at physiological temperature are highly dynamic. In contrast to cryo-EM, which provides three-dimensional (3D) volume data, AFM is restricted to surface analysis. Nevertheless, AFM images molecules in a native-like environment: (i) at ambient temperature, (ii) at ambient pressure, (iii) in physiological buffer and (iv) in membranes (in the case of membrane proteins). Furthermore, the AFM measurement mechanism and the openness of the fluid cell allow for (v) buffer exchanges, (vi), temperature changes and (vii) force changes during image acquisition[2,4].

High-speed AFM (HS-AFM)[5] has an additional advantage in that it yields real-time nanometre topographical information of single biomolecules at unprecedented spatiotemporal resolutions[6–13], through the integration of short cantilevers[14] and the development of faster scanners[15] and feedback operation[16]. Although this is proving powerful in revealing conformational changes of proteins[4,17], it is often not possible to resolve sub-molecular structural features on protein surfaces, primarily owing to the finite size of the AFM tip. For probes typically used to image biological samples, the resolution in the z direction (topography) is about 1 Å, whereas the lateral resolution in the x, y directions is about 1 nm, fundamentally limited by the probe geometry and the probe–sample interaction forces. The lateral resolution is further reduced when imaging softer samples, owing to an increased contact area between the tip and flexible protein structures[18]. Because of these limitations, sub-nanometre lateral resolution of biological samples has only been reported for two-dimensional (2D) crystals[19,20], and was evidenced to be an overestimation due to periodic tip convolution effects[21]. In an attempt to circumvent such limitations, tip deconvolution algorithms were proposed[22,23], which produced sharpened images but could introduce artefacts.

Localization microscopy methods, also known as super-resolution fluorescence microscopies, such as stochastic optical reconstruction microscopy (STORM)[24] and photoactivated localization microscopy (PALM)[3], have provided insights into the architecture and macromolecular assemblies of cells. By isolating and pinpointing the source of excited fluorescence signals with high spatial precision in many images, high-lateral-resolution maps can be reconstructed, taking the ~400 nm resolution limit set by the diffraction limit of light down to about 20 nm (refs. [25,26]).

Here, inspired by these fluorescence localization microscopy methods (Extended Data Fig. 1a–d), we develop LAFM, whereby localization algorithms are applied to the spatial fluctuations of topographic features in AFM and HS-AFM images (Extended Data Fig. 1e–h). Comparisons with X-ray structures and molecular dynamics (MD) simulations show that this approach can reveal angstrom-range high-resolution details on protein surfaces.

Breaking the resolution limit

Under specific conditions; that is, with an atomically sharp tip and rapidly decaying tip–sample interaction forces, atomic resolution is attainable on flat incompressible materials such as mica by conventional AFM imaging[18]. Achieving and maintaining such conditions on biological samples, which are not only soft and dynamic, but also immersed in liquid at room temperature, is not possible. Typically, the tip geometry from the apex up to the height of the objects being imaged is much larger than the separation distance between the features of

[1]Department of Anesthesiology, Weill Cornell Medicine, New York, NY, USA. [2]Department of Physiology and Biophysics, Weill Cornell Medicine, New York, NY, USA. [3]Department of Biochemistry and Molecular Biophysics, Washington University, St. Louis, MO, USA. [4]Present address: School of Physics and Astronomy, University of Leeds, Leeds, UK. ✉e-mail: sis2019@med.cornell.edu

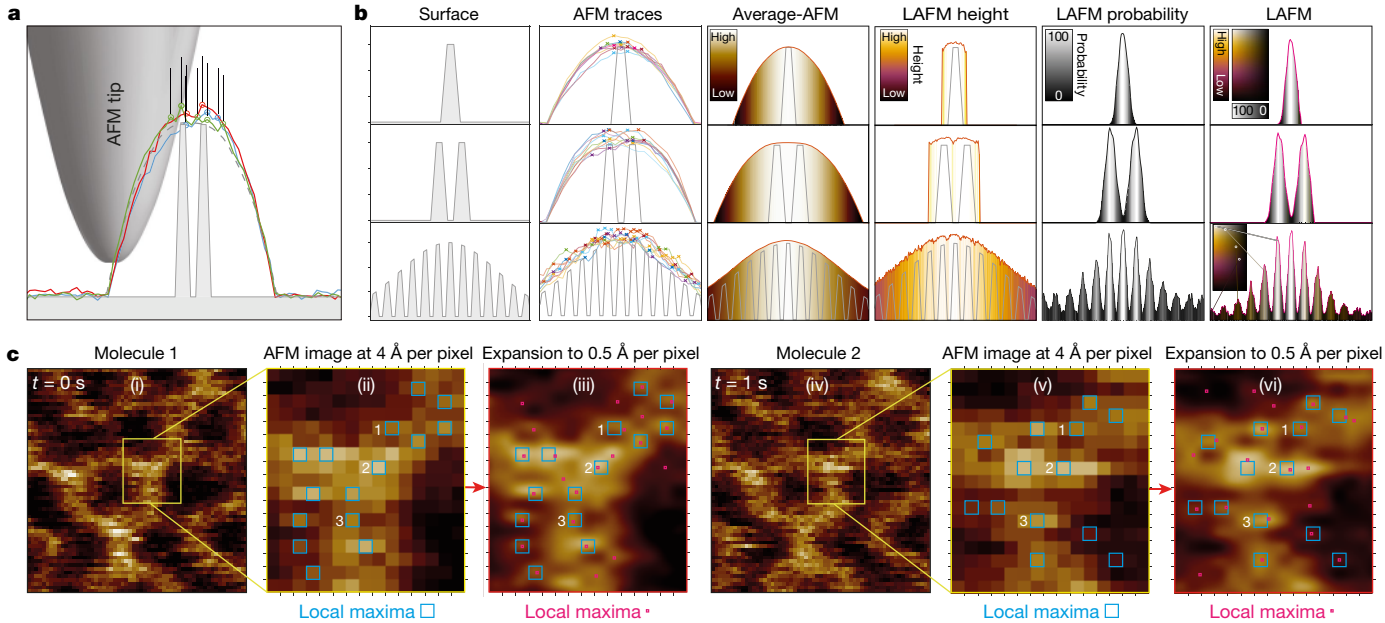

Fig. 1 | Principle of LAFM. a, Schematic of an AFM tip scanning a high topography with high-resolution features. Dashed line, theoretical contour. Coloured lines, three representative simulated topography traces. Open symbols and lines, vertical and lateral positions of detected local maxima. **b**, Simulations (n = 1,000) of the LAFM method on surfaces with one (top), two (middle) and many (bottom) height-modulated surface features. Surface: representation of idealized surface features (grey). AFM traces: nine representative simulated topography traces (coloured lines), with detected local maxima (crosses). Average AFM: average topography (n = 1,000). LAFM height: average height of detected local maxima. LAFM probability: peaking probability distribution of detected local maxima. LAFM: LAFM map merging real-space height with peaking probability. Insets: false-colour scales represent height, probability and height/probability. **c**, High-spatial-resolution topography local maxima detection. (i), (iv), Two representative sequential (t = 0 s, t = 1 s) raw data images of an A5 trimer. (ii), (v), Magnified views of raw data (4 Å per pixel). Blue squares, local maxima pixels. Local maxima labelled '1', '2' and '3' are detected at identical pixel locations in both images. (iii), (vi), Same image regions after image expansion (0.5 Å per pixel). Red squares, local maxima pixels.

interest (Fig. 1a, b, surface). The finite tip radius results in convoluted lateral dimensions. The signal is further obstructed by noise in the z direction and stochastic fluctuations of flexible protein surface features (Supplementary Video 1) in the x, y and z directions (Fig. 1b, AFM traces). Averaging several of these traces removes noise and results in a noise-free topography trace but the tip convolution remains a limiting factor (Fig. 1b, average AFM). By applying localization algorithms that detect the local maxima in the same series of traces (Fig. 1b, AFM traces, crosses), extracting the location-specific heights (Fig. 1b, LAFM height) and merging the individual detections in a peaking-probability map (Fig. 1b, LAFM probability), the surface structures are reconstructed with greater lateral resolution in an LAFM map (Fig. 1b, LAFM). Local peak-search algorithms to identify and accumulate local maxima in AFM data have previously been used to create probability density maps, from which energy landscapes were calculated to sample the conformational space of protein moieties[27] and to derive stiffness maps[7]. Here we build on this concept and extend the approach, leveraging the methodological knowledge generated by the development of super-resolution fluorescence localization microscopies[3,24]. Localization-based fluorescence microscopy methods taught us that a resolution superior to the physical limitations can be achieved when the localization of isolated signals is determined with high spatial precision in many images, which are later merged in a compiled map[3], which has higher lateral resolution than the initial data. Advantage is taken of the fact that the peak position of signals with wide intensity distributions can be determined with astonishing precision. Here, we adapt this transformative rationale to AFM data (Extended Data Fig. 1e–h). First, the pixel- and/or AFM-restricted low-lateral-resolution data are oversampled to allow peak positions to be determined with increased spatial localization resolution. Peak positions are measured and localization data are then merged to give a reconstructed map with higher lateral resolution than the initial pixel sampling and/or technique allowed (Fig. 1b; compare LAFM with average AFM).

The LAFM map reconstruction is best illustrated in the simulation, where several features of varying height are contoured next to each other (Fig. 1b, bottom row). Simulations show that the LAFM algorithm detects features that are hidden to theoretical and average topographies (Fig. 1b, Extended Data Fig. 3). However, the detection probability performs best on flat samples, and is nonlinear with the protrusion height if there are closely neighbouring higher features (Extended Data Fig. 2). Each pixel in these maps contains both height and probability information (Fig. 1b, bottom right). Further simulations with varying tip radius and shape on simple (Extended Data Fig. 4, Supplementary Video 2) and more complex (Extended Data Fig. 5) model 3D surfaces showed that the LAFM algorithm outperformed averaging methods within 10–100 images, showing the greatest improvement in resolution (about 1/5) for tip radii greater than the separation of structural features. These analyses corroborate that the quality of the LAFM map increases with increasing number of observations until it plateaus, at around 50 (for a sharp tip) and around 500 (for a blunt tip) particles are analysed.

On real AFM data, detection of local height maxima is performed after image expansion (Fig. 1c). Image expansion using bicubic interpolation (see Methods) does not increase the lateral resolution of the topography but allows the detection of local maxima with far greater spatial precision (Fig. 1c; compare panels (ii) and (v) with (iii) and (vi)). Merging the high-precision local maxima from several particles results in resolving structural features with separation distances shorter than the initial pixel sampling. To retain the topographic structural information, the topography height value from each peak location is carried into the LAFM reconstruction, where height and peaking probability are encoded by a 2D false-colour scale in which the green/red ratio scales linearly with height h and probability P from white at P = 1 to black at

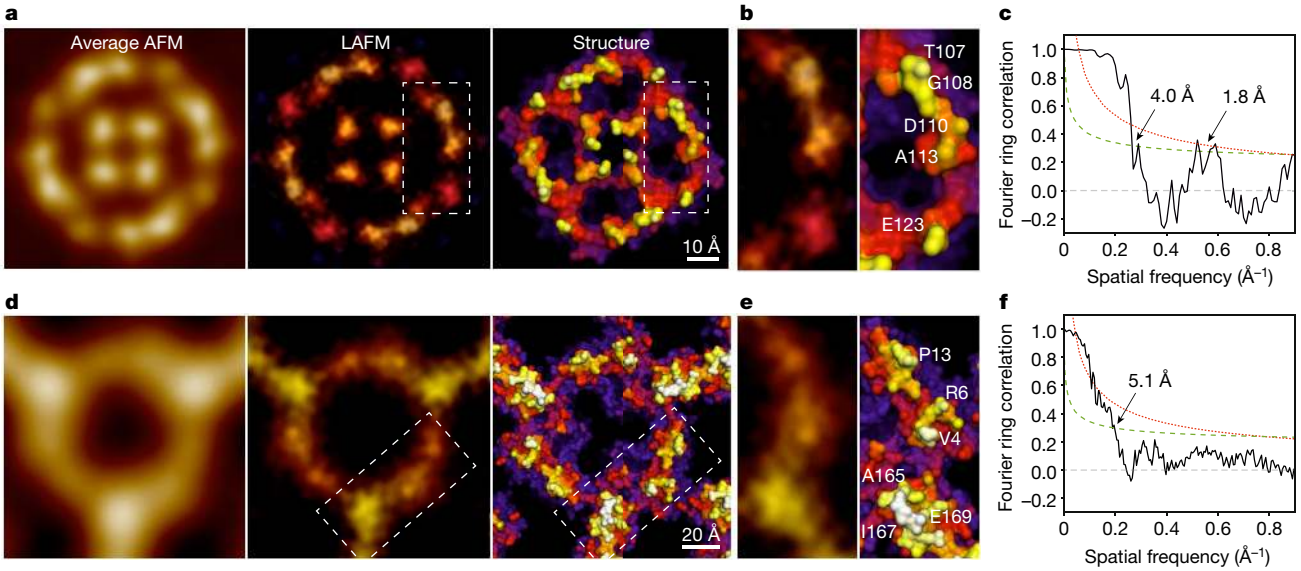

Fig. 2 | LAFM of AqpZ and A5. a–**c**, AqpZ; **d**–**f**, A5. **a**, **d**, Left, average AFM maps; middle, LAFM maps; and right, surface representations of X-ray structures. **b**, **e**, Detail views of LAFM maps and X-ray structures, with recognizable residues labelled. **c**, **f**, FRC analyses of LAFM half-maps. AqpZ data acquisition: AqpZ reconstituted in DMPC/POPC (1/1) membranes imaged by conventional AFM in contact mode; scan speed, 6.8 lines per second; scan area, 169 nm; image size, 512 pixels; pixel sampling, 3.3 Å per pixel[20]. A5 data acquisition: A5 on a DOPC/DOPS (8/2) bilayer imaged by HS-AFM in amplitude modulation mode; scan speed, 1 frame per second; scan area, 80 nm; image size, 200 pixels; pixel sampling, 4.0 Å per pixel. LAFM map pixel sampling, 0.5 Å per pixel; AqpZ: $n = 128$, A5: $n = 698$, filtered to 5 Å. X-ray structures: AqpZ, PDB 2ABM, A5, PDB 1HVD.

$P = 0$ (Extended Data Fig. 1i, j). Furthermore, each peaking detection, originating from an atomic tip–sample interaction, is assigned a 2D Gaussian density function decaying from 1 to 0 over 1.4 Å to approximate atomic solvent-accessible surface areas. A reconstructed LAFM map thus compiles, from many particles, the average topography height refined by the peaking probability (Fig. 1b, right), where each pixel carries the full information about topography and its likelihood of being detected at this location. In merging many particles, randomly distributed apparatus noise does not merge into consistent height/probability data. Conversely, peaking detections that emerge from protein surface fluctuations will merge into strong localized signals in high-resolution reconstructed LAFM maps.

Single amino acids on protein surfaces

To illustrate the power of the LAFM approach, we first applied it to a former conventional AFM dataset[20]. After extraction and alignment of aquaporin-Z (AqpZ) tetrameric channels, the LAFM map revealed details comparable to the surface of the X-ray structure (Fig. 2a, Supplementary Video 3), resolving single amino-acids on surface protruding loops (Fig. 2b). Line profile analysis and image comparison between the average AFM topography, previous peak probability mapping methods[27] and LAFM probability maps of independent dataset half-maps show the ability of LAFM to detect previously hidden structural features (separated by 2.6 Å) well beyond the details resolved by previous averaging and peak probability methods (11 Å) and the Nyquist frequency of the raw data (1/(6.6 Å)) (Extended Data Fig. 6a–i). Interestingly, among the AqpZ X-ray structures, E31 in the central a-loop is in different orientations, and the LAFM map indicates that in physiological buffer the E31 rotamer configuration, as found in PDB 2ABM, is preferred (Extended Data Fig. 6j). We also applied the LAFM approach to annexin-V (A5) trimers extracted from HS-AFM videos[5,9,28] (Fig. 2d, Supplementary Video 4) and found that the LAFM map resolved fine structural details (whereas the average resolved only the protein envelope) along the backbone of the molecule (Fig. 2b).

To quantitatively assess the resolution of the LAFM maps, we applied the Fourier ring correlation (FRC) method, developed for electron microscopy[29] and more recently adapted for super-resolution fluorescence microscopy[26]. The FRC method splits the datasets into halves and assesses their statistical resemblance as a function of the resolution range. This analysis resulted in a resolution of 4.0 Å for AqpZ, 5.1 Å for A5 and 4.5 Å for A5 P13W-G14W (Fig. 2c, f, Extended Data Fig. 7a, b, h). The FRC curve of AqpZ has, in addition to the signal power up to about 4.0 Å, a second information-containing range in the 2-Å regime. Thus, both the real-space (Extended Data Fig. 6h, i) and the statistical analysis of AqpZ LAFM half-maps report resolution at distances shorter than the Nyquist frequency of the raw data. Accordingly, LAFM maps of both AqpZ and A5 resolve details down to the amino acid size range (around 5 Å to 4 Å), and some signal power on the quasi-atomic scale (around 2 Å) in the case of AqpZ (Fig. 2b, c, Extended Data Fig. 6). We also capitalized on the serendipitous co-existence of two differently oriented A5 trimers in the A5 lattice. LAFM of the two trimer datasets, independent from each other and acquired through different relative AFM scan-directions, agree in great detail (Extended Data Fig. 7c–e). Finally, we cloned, expressed and purified a mutant A5, replacing two amino acids in the N terminus with tryptophans (P13W, G14W), and imaged the A5-mutant by HS-AFM (Extended Data Fig. 7f–h). LAFM maps of the A5 mutant show overall rearrangements of the N terminus with increased height and peaking probability at the mutation site.

Localization AFM of CLC antiporters

The AFM data of A5 and AqpZ were acquired on 2D lattices, however, a considerable advantage of LAFM is that the biomolecules do not need to be confined in a crystal for analysis, but can be sparsely populating a native-like environment. Furthermore, the buffer conditions inside the fluid cell can be changed to assess structural changes in response to environmental changes. Therefore, we studied CLC-ec1 (a Cl^-/H^+ antiporter from *E. coli*)[30,31], which, to our knowledge, has not been observed by AFM, and whose transport mechanism remains unresolved. Mutations in human CLC family homologues have been associated with diseases[32].

HS-AFM of CLC-ec1 in membranes formed through proteo-liposome fusion showed a dispersed population of proteins protruding 1.2 nm

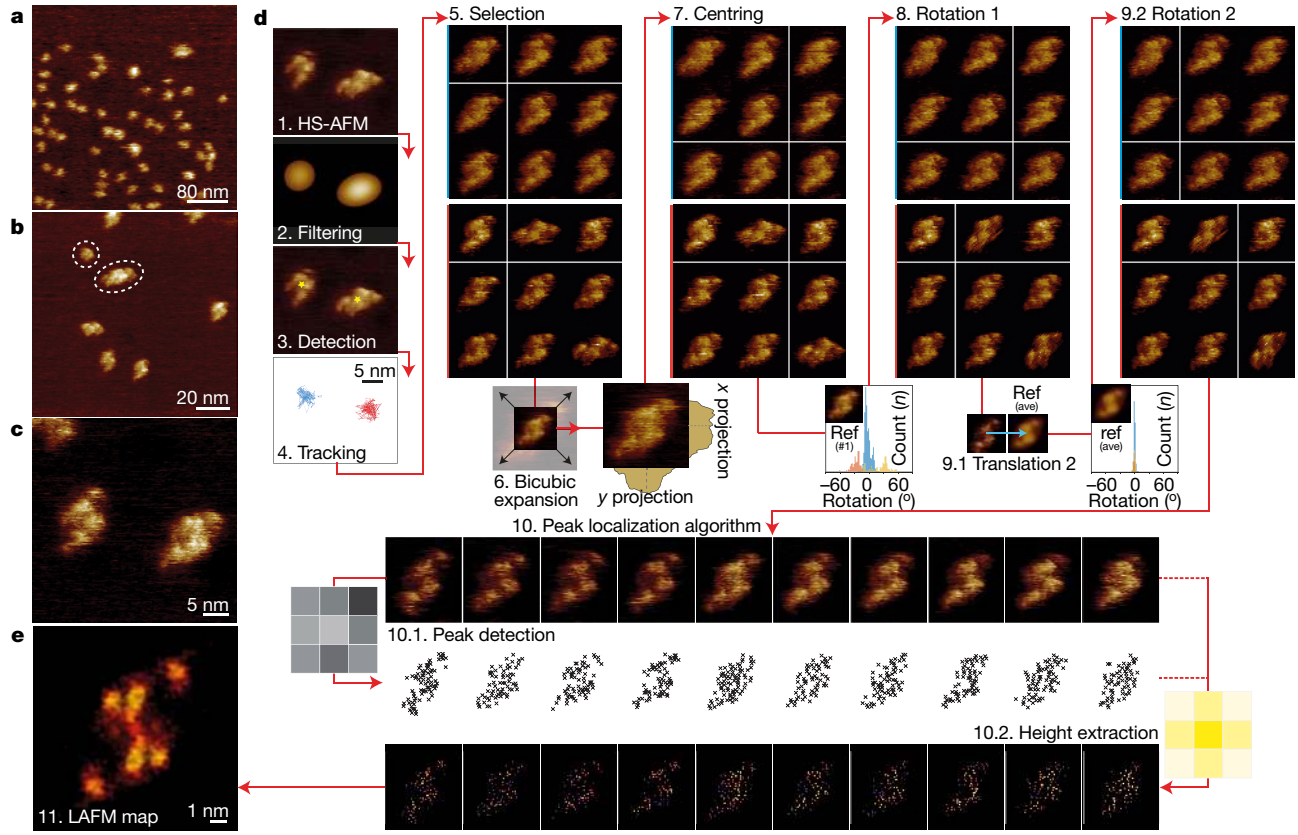

Fig. 3 | HS-AFM imaging and LAFM workflow of CLC-ec1. a–**c**, HS-AFM images of CLC-ec1 in a POPE:POPG (2:1 w-w) membrane at 400 nm (300 pixels) (**a**), 120 nm (300 pixels) (**b**) and 40 nm (300 pixels) (**c**) image (frame) size of predominantly dimeric CLC-ec1 at low density in a membrane. **d**, LAFM method workflow steps: (1) HS-AFM video acquisition; (2) image Gaussian filtering; (3) molecule detection; (4) 2D tracking to separate single molecules (molecules highlighted blue or red can be treated individually); (5) molecule selection; (6) bicubic expansion (original pixel sampling, 1.33 Å per pixel; expanded pixel sampling, 0.5 Å per pixel); (7) molecule centring (first round) by centre of mass; (8) rotational alignment (first round) of molecules through rotational cross-correlation with a reference frame, ref(#1); (9) translational and rotational alignment (second round) through cross-correlation with the average molecule, ref(ave), from step 8 (inset histograms, rotation angle distributions for all particles in steps 8 and 9); (10) LAFM method; insets: aligned HS-AFM images ($n = 200$); (10.1) LAFM peak detection of local maxima; (10.2) height extraction at each peak position and application of a 1.4-Å localization probability distribution; (11) LAFM map reconstruction through merging of all LAFM detections.

from the membrane (Fig. 3a–c, Supplementary Video 5). CLC-ec1 was predominantly dimeric, with small populations of monomers and higher-order oligomers assembled from multiple dimers (Fig. 3b). The topography and lateral dimensions of the dimers (Fig. 3c) were consistent with the 5.5 nm × 9.6 nm dimensions of the extracellular face of CLC-ec1 (Extended Data Fig. 8a–e)[33,34]. Because the dimers were not confined, they exhibited translational and rotational freedom (Fig. 3c, Supplementary Video 5), which led us to establish a generalized LAFM workflow (Fig. 3d; see Methods): (1) a HS-AFM video is acquired and (2) low-pass-filtered, so that (3) particles can automatically be detected. Particles are thus (4) tracked throughout the HS-AFM observation and (5) selected and extracted in a gallery. (6) Bicubic image expansion allows for (7) precise particle centring and (8) rotational alignment to an arbitrary molecule reference. A second cycle of (9.1) lateral and (9.2) rotational alignment, this time with respect to an ensemble average, prepares particles for (10) application of the LAFM method (Supplementary Video 6). As described in Fig. 1, (10.1) local maxima peaks are detected and (10.2) the height at these locations is extracted with a 1.4-Å-wide probability radius. Finally, all detections are merged in a height–probability LAFM map (Fig. 3e). The particle gallery (step 5) can be assembled from many molecule observations in one or several frames. Alternatively, an LAFM map can be reconstructed from one molecule observed over time, which gives this method unique possibilities to access high-resolution information of individual molecules.

Conformational changes in CLC-ec1

The exchange pathway in the CLC-ec1 Cl^-/H^+-antiporter has been proposed to have two separate entrances/exits for H^+ and Cl^- on the intracellular face, converging to a central binding region from which both ions follow the same path to the extracellular side. However, there is debate about whether the gating mechanism requires only localized side-chain motions in the Cl^- pathway based on X-ray structures, or if greater movements occur, as evidenced by nuclear magnetic resonance (NMR)[35,36], computational[37] and helix-crosslinking studies[38]. Findings by these non-crystallographic methods[35–39] have led to suggestions that confinement of CLC in 3D lattices inhibit large conformational movements (Extended Data Table 1, Extended Data Fig. 8f), similar to other transporters[40–43]. Cl^- transport by CLC-ec1 is maximal at acidic pH and stalled at neutral and basic pH (owing to pH-dependent activation and lack of H^+ as substrate)[44]. A more recent structure of a protonation-mimicking triple mutant also indicates conformational rearrangements[45]. Therefore, we performed HS-AFM of transporters sparsely packed in lipid membranes and in physiological buffer. Subsequent LAFM of the pH 7.6 (inactive state) and pH 4.5 (active state) observations should inform on whether large-scale conformational changes occur.

On the basis of the X-ray structure surface (Fig. 4a), we assigned the protruding residues expected to give signals in AFM: Asp73 in loop B-C, Glu235, Asp240 and Lys243 in the long loop I–J, Asn327 in loop

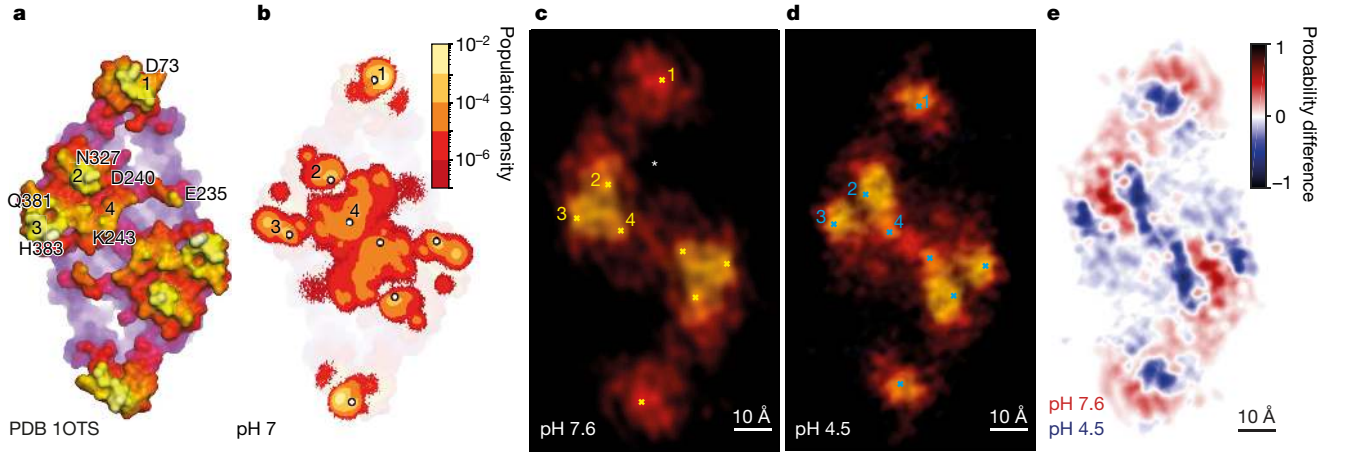

Fig. 4 | Conformational changes in CLC-ec1 at neutral and acidic pH. **a**, Extracellular surface of CLC-ec1 at pH 9.5 (PDB 1OTS[31]); membrane-protruding residues in four major protrusions (1–4) are labelled. **b**, Logarithmic-scale population density map of the positions of atoms with the highest *z* coordinates on the extracellular surface of CLC-ec1 from 5.6-μs MD simulations at pH 7 (simulated from PDB 1OTS). Major protrusions (1–4) are labelled. Major contributions to each population peak: (1) D73 (97%), A72 (2.7%); (2) N237 (91%), D240 (2.2%); (3) Q381 (42.3%), H383 (54.7%); (4) K243 (52%), D240 (21.7%), S245 (3.4%). **c**, **d**, LAFM reconstructions of CLC-ec1 at pH 7.6 (**c**) and pH 4.5 (**d**). The ion pathway entry is labelled with an asterisk. The four major protrusions (1–4) are highlighted for comparison with the X-ray structure and the MD population density map. **e**, Detection probability difference map between CLC-ec1 LAFM reconstructions at pH 7.6 (**c**) and pH 4.5 (**d**). The difference map highlights the conformational changes of the four major protrusions, notably a ~6-Å movement of peak 1 towards the dimer axis.

L–M, and Gln381 and His383 in loop N–O. To refine the interpretation of LAFM reconstructions, we used MD simulations to convert the static X-ray structure into a dynamic molecular system fluctuating at room temperature and at pH 7 (Supplementary Video 1). Similar to the LAFM method, we plotted a population density map of the distribution of the *z*-coordinate local maxima on the CLC-ec1 extracellular face from MD trajectories, which reflected side-chain motions of membrane-protruding residues (Fig. 4b, Extended Data Fig. 8g, h). The MD trajectories show how structural fluctuations that are probed (in AFM) and merged (in LAFM) allow extraction of high-resolution information of amino acid residues on protein surfaces.

The CLC-ec1 LAFM reconstructions at pH 7.6 and pH 4.5 display the same set of structural features as the X-ray structure and the MD population map, but in distinctly different configurations (Fig. 4c, d). Peaks 2, 3 and 4, which form a triangle close to the dimer interface, pack more loosely at pH 4.5, and peak 3 moves towards a more lateral position on the dimer, while the most remarkable conformational change is a ~6-Å movement of peak 1 towards the dimer interface at acidic pH. The extracellular Cl^-/H^+ ion pathway lies between Asp73, Asn327 and Glu235 (Fig. 4c, asterisk); thus, under the premise that these displacements are related to movements in the underlying helices, these structural changes might alter accessibility to the extracellular gate. In summary, LAFM reports large pH-dependent conformational changes (Fig. 4e, Supplementary Video 7).

By recording 3D topographic images and videos, AFM and HS-AFM offer rich data, captured through many atomic interactions between tip and sample in liquid and at ambient conditions. By pinpointing peak interaction locations with high spatial precision in oversampled topographies, LAFM produces quasi-atomic resolution maps of protein surfaces from such data. We demonstrate the ability of LAFM to detect amino acid side chains on the surfaces of AqpZ, A5 and CLC-ec1, mutation-related differences in A5, and conformational changes in the angstrom range in CLC-ec1. Our LAFM maps, calculated from CLC-ec1 imaged at physiological and acidic pH, identified substantial differences in the central region, where helices N and O are located, and at the peripheral end of helix B, which moves towards the dimer centre, giving the entire molecule a ~1.2-nm shortened appearance (Fig. 4d, e).

HS-AFM[5] operates in amplitude modulation mode using short cantilevers that oscillate at resonance at around 660 kHz (oscillation cycle of around 1.5 μs). The tip touches the surface only during ~10% of an oscillation cycle[4], thus about 150 ns. Even though this is a short period in the life of a protein, side-chain fluctuations occur in such time regimes, thus blurring the signal. Hence, LAFM will provide improved data when the next generation of faster HS-AFM systems arrive. Today, amplitude detectors oversample the cantilever[5,46], but feedback operation and the *z*-piezo are limiting (about 100 kHz) factors and need improvement.

The LAFM method can be used in two different ways: LAFM maps can be reconstructed (i) from many molecules recorded in one or several frames or (ii) from a single molecule over time. The first approach allows us to resolve time- or environment-dependent conformational changes. About 50 particles are needed to reconstruct an LAFM map (Extended Data Fig. 5); therefore, the temporal resolution of LAFM is decreased to the time required to accumulate these 50 observations. Faster HS-AFM operation will of course improve time-resolved studies of single molecules. Alternatively, imaging densely packed proteins (with around 50 particles in each frame[8,47]) would allow LAFM map reconstruction of the conformation of the proteins in each frame, giving high-resolution structural changes as a function of time. The second approach gives the method the unique capability to provide high-resolution information of single molecules or of non-ordered supramolecular assemblies. Altogether, we envisage that LAFM will become the standard method applied to AFM imaging, allowing the extraction of high-resolution information beyond the tip-radius resolution limit in the study of single biomolecules in native-like environments.

Online content

Any methods, additional references, Nature Research reporting summaries, source data, extended data, supplementary information, acknowledgements, peer review information; details of author contributions and competing interests; and statements of data and code availability are available at https://doi.org/10.1038/s41586-021-03551-x.

1. Binnig, G., Quate, C. F. & Gerber, C. Atomic force microscope. *Phys. Rev. Lett.* **56**, 930–933 (1986).
2. Heath, G. R. & Scheuring, S. Advances in high-speed atomic force microscopy (HS-AFM) reveal dynamics of transmembrane channels and transporters. *Curr. Opin. Struct. Biol.* **57**, 93–102 (2019).

3. Betzig, E. et al. Imaging intracellular fluorescent proteins at nanometer resolution. *Science* **313**, 1642–1645 (2006).
4. Lin, Y. C. et al. Force-induced conformational changes in PIEZO1. *Nature* **573**, 230–234 (2019).
5. Ando, T. et al. A high-speed atomic force microscope for studying biological macromolecules. *Proc. Natl Acad. Sci. USA* **98**, 12468–12472 (2001).
6. Kodera, N., Yamamoto, D., Ishikawa, R. & Ando, T. Video imaging of walking myosin V by high-speed atomic force microscopy. *Nature* **468**, 72–76 (2010).
7. Preiner, J. et al. High-speed AFM images of thermal motion provide stiffness map of interfacial membrane protein moieties. *Nano Lett.* **15**, 759–763 (2015).
8. Ruan, Y. et al. Structural titration of receptor ion channel GLIC gating by HS-AFM. *Proc. Natl Acad. Sci. USA* **115**, 10333–10338 (2018).
9. Heath, G. R. & Scheuring, S. High-speed AFM height spectroscopy reveals µs-dynamics of unlabeled biomolecules. *Nat. Commun.* **9**, 4983 (2018).
10. Nievergelt, A. P., Banterle, N., Andany, S. H., Gönczy, P. & Fantner, G. E. High-speed photothermal off-resonance atomic force microscopy reveals assembly routes of centriolar scaffold protein SAS-6. *Nat. Nanotechnol.* **13**, 696–701 (2018).
11. Eeftens, J. M. et al. Condensin Smc2-Smc4 dimers are flexible and dynamic. *Cell Rep.* **14**, 1813–1818 (2016).
12. Shibata, M. et al. Oligomeric states of microbial rhodopsins determined by high-speed atomic force microscopy and circular dichroic spectroscopy. *Sci. Rep.* **8**, 8262 (2018).
13. Nasrallah, H. et al. Imaging artificial membranes using high-speed atomic force microscopy. *Methods Mol. Biol.* **1886**, 45–59 (2019).
14. Viani, M. B. et al. Fast imaging and fast force spectroscopy of single biopolymers with a new atomic force microscope designed for small cantilevers. *Rev. Sci. Instrum.* **70**, 4300–4303 (1999).
15. Kodera, N., Yamashita, H. & Ando, T. Active damping of the scanner for high-speed atomic force microscopy. *Rev. Sci. Instrum.* **76**, 053708 (2005).
16. Kodera, N., Sakashita, M. & Ando, T. Dynamic proportional-integral-differential controller for high-speed atomic force microscopy. *Rev. Sci. Instrum.* **77**, 083704 (2006).
17. Shibata, M. et al. Real-space and real-time dynamics of CRISPR-Cas9 visualized by high-speed atomic force microscopy. *Nat. Commun.* **8**, 1430 (2017).
18. Gan, Y. Atomic and subnanometer resolution in ambient conditions by atomic force microscopy. *Surf. Sci. Rep.* **64**, 99–121 (2009).
19. Müller, D. J., Schabert, F. A., Büldt, G. & Engel, A. Imaging purple membranes in aqueous solutions at sub-nanometer resolution by atomic force microscopy. *Biophys. J.* **68**, 1681–1686 (1995).
20. Scheuring, S. et al. High resolution AFM topographs of the *Escherichia coli* water channel aquaporin Z. *EMBO J.* **18**, 4981–4987 (1999).
21. Fechner, P. et al. Structural information, resolution, and noise in high-resolution atomic force microscopy topographs. *Biophys. J.* **96**, 3822–3831 (2009).
22. Markiewicz, P. & Goh, M. C. Atomic force microscopy probe tip visualization and improvement of images using a simple deconvolution procedure. *Langmuir* **10**, 5–7 (1994).
23. Bukharaev, A. A., Bukharaev, A. A., Berdunov, N. V, Ovchinnikov, D. V. & Salikhov, K. M. Three-dimensional probe and surface reconstruction for atomic force microscopy using a deconvolution algorithm. *eCM J.* **12**, 225 (1998).
24. Rust, M. J., Bates, M. & Zhuang, X. Sub-diffraction-limit imaging by stochastic optical reconstruction microscopy (STORM). *Nat. Methods* **3**, 793–796 (2006).
25. Small, A. & Stahlheber, S. Fluorophore localization algorithms for super-resolution microscopy. *Nat. Methods* **11**, 267–279 (2014); corrigendum **11**, 971 (2014).
26. Nieuwenhuizen, R. P. J. et al. Measuring image resolution in optical nanoscopy. *Nat. Methods* **10**, 557–562 (2013).
27. Scheuring, S., Müller, D., Stahlberg, H., Engel, H.-A. & Engel, A. Sampling the conformational space of membrane protein surfaces with the AFM. *Eur. Biophys. J.* **31**, 172–178 (2002).
28. Miyagi, A., Chipot, C., Rangl, M. & Scheuring, S. High-speed atomic force microscopy showsthat annexin V stabilizes membranes on the second timescale. *Nat. Nanotechnol.* **11**, 783–790 (2016).
29. Saxton, W. O. & Baumeister, W. The correlation averaging of a regularly arranged bacterial cell envelope protein. *J. Microsc.* **127**, 127–138 (1982).
30. Accardi, A. & Miller, C. Secondary active transport mediated by a prokaryotic homologue of ClC Cl^- channels. *Nature* **427**, 803–807 (2004).
31. Dutzler, R., Campbell, E. B. & MacKinnon, R. Gating the selectivity filter in ClC chloride channels. *Science* **300**, 108–112 (2003).
32. Jentsch, T. J. & Pusch, M. CLC chloride channels and transporters: structure, function, physiology, and disease. *Physiol. Rev.* **98**, 1493–1590 (2018).
33. Accardi, A. et al. Separate ion pathways in a Cl^-/H^+ exchanger. *J. Gen. Physiol.* **126**, 563–570 (2005).
34. Dutzler, R., Campbell, E. B., Cadene, M., Chait, B. T. & MacKinnon, R. X-ray structure of a ClC chloride channel at 3.0 Å reveals the molecular basis of anion selectivity. *Nature* **415**, 287–294 (2002).
35. Abraham, S. J. et al. 13C NMR detects conformational change in the 100-kD membrane transporter ClC-ec1. *J. Biomol. NMR* **61**, 209–226 (2015).
36. Khantwal, C. M. et al. Revealing an outward-facing open conformational state in a CLC Cl^-/H^+ exchange transporter. *eLife* **5**, e11189 (2016).
37. Miloshevsky, G. V., Hassanein, A. & Jordan, P. C. Antiport mechanism for Cl^-/H^+ in ClC-ec1 from normal-mode analysis. *Biophys. J.* **98**, 999–1008 (2010).
38. Basilio, D., Noack, K., Picollo, A. & Accardi, A. Conformational changes required for H^+/Cl^- exchange mediated by a CLC transporter. *Nat. Struct. Mol. Biol.* **21**, 456–463 (2014).
39. Osteen, J. D. & Mindell, J. A. Insights into the ClC-4 transport mechanism from studies of Zn^{2+} inhibition. *Biophys. J.* **95**, 4668–4675 (2008).
40. Reyes, N., Ginter, C. & Boudker, O. Transport mechanism of a bacterial homologue of glutamate transporters. *Nature* **462**, 880–885 (2009).
41. Ruan, Y. et al. Direct visualization of glutamate transporter elevator mechanism by high-speed AFM. *Proc. Natl Acad. Sci. USA* **114**, 1584–1588 (2017).
42. Krishnamurthy, H. & Gouaux, E. X-ray structures of LeuT in substrate-free outward-open and apo inward-open states. *Nature* **481**, 469–474 (2012).
43. Hofmann, S. et al. Conformation space of a heterodimeric ABC exporter under turnover conditions. *Nature* **571**, 580–583 (2019).
44. Accardi, A., Kolmakova-Partensky, L., Williams, C. & Miller, C. Ionic currents mediated by a prokaryotic homologue of CLC Cl channels. *J. Gen. Physiol.* **123**, 109–119 (2004).
45. Chavan, T. S. et al. A CLC-ec1 mutant reveals global conformational change and suggests a unifying mechanism for the Cl^-/H^+ transport cycle. *eLife* **9**, e53479 (2020).
46. Miyagi, A. & Scheuring, S. A novel phase-shift-based amplitude detector for a high-speed atomic force microscope. *Rev. Sci. Instrum.* **89**, 083704 (2018).
47. Marchesi, A. et al. An iris diaphragm mechanism to gate a cyclic nucleotide-gated ion channel. *Nat. Commun.* **9**, 3978 (2018).

Methods

HS-AFM

HS-AFM measurements (annexin-V, CLC-ec1) were taken with an amplitude modulation mode HS-AFM (RIBM), as previously described in ref. [28]. In brief, we used short cantilevers (USC-F1.2-k0.15, NanoWorld) with a spring constant of 0.15 N m^{-1}, a resonance frequency of ~0.66 MHz and a quality factor of ~1.5 in buffer.

AFM

AFM data (aquaporin-Z) were taken by contact-mode AFM using a Nanoscope-III AFM (Digital Instruments) equipped with a 120-µm scanner (J-scanner) and oxide-sharpened Si_3N_4 cantilevers with a length of 120 µm and spring constant of 0.1 N m^{-1} (Olympus Ltd), as detailed in ref. [20].

Cloning, expression and purification of annexin-V-P13W-G14W

The P13W-G14W site-directed mutagenesis was performed on an untagged human annexin pET28a expression vector using the Q5 site-directed mutagenesis kit (New England BioLabs) and the following mutagenic primers (mutated nucleotides are in bold): 5′-GACCGATTTT**TGGTGG**TTTGATGAACGTGCTGATGCC-3′ and 5′-ACGGTACCACGCAGCACTTG-3′.

The mutated genes were sequenced to confirm that only the desired mutations were inserted into the plasmid. The annexin-V-P13W-G14W plasmid was then transformed into BL21 (DE3) pLysE chemically competent *E. coli* cells (Invitrogen), and grown overnight at 37 °C for small-scale culture. The overnight culture (50 ml) was inoculated into 2 l fresh Luria–Bertani broth media at 37 °C, and once an optical density (A600) of 0.6–0.8 was achieved, the cells were induced by addition of 0.4 mM isopropyl β-D-1-thiogalactopyranoside. After induction for 4 h, the cells were separated from the culture medium by centrifugation (5,000 g; 20 min) and resuspended in ice-cold calcium buffer (50 mM Tris pH 7.5, 10 mM $CaCl_2$). The suspension was three times tip-sonicated on ice for 5 min (one pulse every 9 s), and centrifuged (23,000 g; 45 min). The supernatant was discarded, and the pellet was resuspended in ice-cold EGTA buffer (50 mM Tris pH 7.5, 60 mM EGTA). After gentle shaking for 30 min, the cell debris were removed by centrifugation (23,000 g; 45 min), and the supernatant containing the soluble Annexin-V-P13W-G14W was dialysed overnight against buffer A (20 mM Tris pH 7.5, 20 mM NaCl). The solution was applied to a HiTrap DEAE FF sepharose column (5 ml) ÄKTA Avant (GE Healthcare Life Sciences), and eluted with a linear gradient of 0–1 M NaCl. Fractions containing annexin-V-P13W-G14W (based on SDS–PAGE analysis) were concentrated to ~1 mg ml^{-1} using 10 kDa centrifugal filters (Amicon, Millipore), and subjected to a final purification step with a Superdex 200 Increase 10/300 gel filtration column (equilibrated with 20 mM Tris pH 7.5, 100 mM NaCl buffer), reaching a final purity of >95% according to SDS–PAGE analysis.

CLC-ec1 expression and purification

Expression and purification of CLC-ec1 were carried out as previously described[48]. BL21-AI *E. coli* competent cells (Thermo Fisher Scientific) were transformed with the plasmid and then 2 l Terrific Broth supplemented with ampicillin was inoculated and grown at 37 °C. Protein expression was induced with anhydro-tetracycline at OD_{600} = 1.0. After 3 h of induction, cells were harvested, then lysed by sonication in buffer supplemented with 5 mM reducing agent TCEP (Tris(2-carboxyethyl) phosphine; Soltec Bioscience) and pH adjusted to 7.5. Protein extraction was carried out with 2% *n*-decyl-β-D-maltopyranoside (DM; Anatrace) for 2 h at room temperature. Cell debris was pelleted down, and the supernatant was run on a 2 ml column volume (CV) TALON cobalt affinity resin (Clontech Laboratories) equilibrated in cobalt column wash buffer (CoWB)/TCEP: 100 mM NaCl, 20 mM Tris, 1 mM TCEP, pH 7.5 with NaOH, 5 mM DM. After binding, the column was washed with 15 CVs of CoWB/TCEP followed by a low-imidazole wash of CoWB/TCEP containing 20 mM imidazole (Sigma-Aldrich). CLC-ec1 was eluted with CoWB/TCEP containing 400 mM imidazole, then concentrated in 30-kDa nominal molecular weight limit (NMWL) centrifugal filters (Amicon, EMD Millipore) to ~500 µl and injected on a Superdex 200 10/30 GL size exclusion column (GE Healthcare) equilibrated in size exclusion buffer (SEB): 150 mM NaCl, 20 mM MOPS pH7.5, 5 mM analytical-grade DM, attached to a medium-pressure chromatography system (NGC, Bio-Rad).

CLC-ec1 reconstitution and bilayer formation

Lipids were resuspended in 300 mM KCl, 20 mM citrate pH 4.5 with NaOH. CHAPS (35 mM) solubilized lipids were combined with protein at 100 µg CLC-ec1 per 1 mg of lipids, corresponding to a protein/lipid mole fraction of 7.6×10^{-4} (assuming a 50% incorporation yield)[48]. The protein–lipid–detergent mixture was dialysed in cassettes (NMWL 10 kDa; ThermoFisher Scientific) at 4 °C against 4 l of buffer for 48 h with buffer changes every 8–12 h. After completion of dialysis, the proteo-liposomes were harvested from the cassettes, freeze/thawed and then extruded using an Avanti Polar Lipids Mini Extruder (Alabaster) through a 400-nm membrane. 1.5 µl of the SUV solution with a total lipid concentration of 0.1 mg ml^{-1} was deposited onto freshly cleaved mica to form supported lipid bilayers (SLBs) through vesicle fusion. The excess lipids, after SLB formation, were rinsed first with deionized water, followed by buffer. For experiments at pH 7.6 the sample was rinsed with 25 mM Tris, 300 mM KCl pH 7.6.

Image expansion

AFM topography images were expanded using bicubic interpolation (Catmull–Rom interpolation; implemented in imageJ, scripted using the method of Burger and Burge)[49]. The method considers values over a 16-pixel surface (4 × 4 pixels) to calculate the new intermediate surface, $p(x, y)$, created by expansion across the central 2 × 2 area. The interpolated values are approximated by 3rd-order polynomials in both the x and y directions:

$$p(x,y) = \sum_{i=0}^{3} \sum_{j=0}^{3} a_{ij} x^i y^j,$$

where i and j are the order of the polynomial for x and y, respectively, and a_{ij} are 16 possible corresponding coefficients. The resulting polynomial can be calculated using the values at the four corners of the central 2 × 2 grid ($f(x, y)$), the gradients at each of those positions in the x and y directions ($f_x(x, y)$, $f_y(x, y)$) and the cross-derivatives ($f_{xy}(x, y)$) requiring the 4 × 4 pixel grid, with the derivatives being calculated numerically. The interpolated surface, $p(x, y)$, between four corner pixels can be described by:

$$p(x,y) = [1\ x\ x^2\ x^3] \begin{bmatrix} a_{00} & a_{01} & a_{02} & a_{03} \\ a_{10} & a_{11} & a_{12} & a_{13} \\ a_{20} & a_{21} & a_{22} & a_{23} \\ a_{30} & a_{31} & a_{32} & a_{33} \end{bmatrix} \begin{bmatrix} 1 \\ y \\ y^2 \\ y^3 \end{bmatrix},$$

where the 16 coefficients can be calculated using the values and derivatives at the four corners:

$$\begin{bmatrix} a_{00} & a_{01} & a_{02} & a_{03} \\ a_{10} & a_{11} & a_{12} & a_{13} \\ a_{20} & a_{21} & a_{22} & a_{23} \\ a_{30} & a_{31} & a_{32} & a_{33} \end{bmatrix} = \begin{bmatrix} 1 & 0 & 0 & 0 \\ 0 & 0 & 1 & 0 \\ -3 & 3 & -2 & -1 \\ 2 & -2 & 1 & 1 \end{bmatrix}$$

$$\begin{bmatrix} f(0,0) & f(0,1) & f_y(0,0) & f_y(0,1) \\ f(1,0) & f(1,1) & f_y(1,0) & f_y(1,1) \\ f_x(0,0) & f_x(0,1) & f_{xy}(0,0) & f_{xy}(0,1) \\ f_x(1,0) & f_x(1,1) & f_{xy}(1,0) & f_{xy}(1,1) \end{bmatrix} \begin{bmatrix} 1 & 0 & -3 & 2 \\ 0 & 0 & 3 & -2 \\ 0 & 1 & -2 & 1 \\ 0 & 0 & -1 & 1 \end{bmatrix}.$$

Using this method, all our datasets were resampled to 0.5 Å per pixel, as indicated in the figure captions. The reason for expanding to 0.5 Å per pixel is based on approximating the picked maxima features to the solvent-accessible surface of atoms with Gaussian profiling, as detailed in the Methods section 'Detection probability'. By constructing the interpolant value from continuous piecewise polynomials, the result is always continuous. This works particularly well for interpolation of smooth areas, as in the case of tip-radius-limited imaging, and therefore considerably improves local maxima localization, but does not increase image resolution.

Detection of local maxima

A local maximum position (Fig. 1c) is defined if a given pixel is higher than all the surrounding eight pixels in a 3 × 3 pixel grid (Figs. 1c, 3d). This 3 × 3 pixel grid is 'scanned' pixel by pixel over the image, and thus all pixels (with the exception of those at the image borders) in each particle image are checked for maxima. To reduce the selection of maxima due to noise in certain datasets, a noise tolerance algorithm that selects maxima based on their prominence above surrounding maxima was implemented. The prominence of each maximum, p_i, is calculated by the following steps: (i) search for the closest neighbouring maximum h_n with higher height than the current maximum h_i or closest image boundary; (ii) find the minimum height along the profile between h_i and h_n or between h_i and the image boundary; and (iii) define the peak prominence as:

$$p_i = h_i - h_{\min}(h_i \to h_n).$$

In our method, for a local maximum to be selected, its prominence must be greater than the noise tolerance (typically 1–2 Å). In our plugin, the noise tolerance is defined by the user from 0 to 100%, where the noise tolerance parameter corresponds to the range of height values from lowest to highest in the image. These maxima selection criteria are based on the noise level of the AFM imaging and the typical root-mean-square fluctuations at protein surfaces (Extended Data Fig. 8g, h). An alternative method is to apply a Gaussian filter to the image to reduce noise and use 0% noise tolerance. The repulsive interaction forces between the farthest exposed atoms of the tip and the atoms in protein moieties that protrude most have very steep separation distance dependence. Very strong short-range interactions occur, including Pauli repulsion and van der Waals, hydration, steric and ionic forces, which depend on the surface properties of both the AFM tip and the protein[50]. As a result, the most exposed atoms dominate local topographic detection and high-resolution information can be obtained through merging many tip–sample atomic interactions at different localizations and time points or on different molecules of the same kind.

Detection probability

The peaking probability at a given localization in an LAFM map, is the cumulative probability that a pixel (in the expanded image) is detected within all particles analysed. It is the sum of: picking events (n), multiplied by the power of the 2D Gaussian, $g(0 < P < 1)$ on each pixel, divided by the total number of particles merged (N).

$$P_{x,y} = \frac{\sum_{i=1}^{N} n_{xi,yi} g_{x,y}}{N}.$$

The 2D Gaussian in all our datasets was set to 1.4 Å width to approximate the solvent-accessible surface of the underlaying atoms (the solvent-accessible surface area is defined as the surface traced out by the centre of a water sphere rolled over the protein atoms)[51] while imparting a continuous probability density to each discreetly selected maximum. The application of larger Gaussian radii to approximate the atomic origin of the tip–sample interactions or pre-filtering the data before peaking leads to loss of resolution or loss of peaking detection of lower features, respectively (Extended Data Fig. 9). Because AFM can reproducibly image atoms on solid surfaces, for example, on mica, the piezo-elements that mediate the scanning of the AFM sample stage have sub-atomic x–y position precision.

Height extraction

The real-space topographic height is extracted at each detection to produce a set of N matrices containing height values for each value of n. This matrix is then false-coloured to allow distinction between height and probability information.

Merging height and detection probability

The false-coloured extracted height values in each image are then multiplied by the greyscale probability values in each image, and then averaged for the whole image set to reconstruct an LAFM map.

LAFM workflow

The HS-AFM videos were 1st-order flattened to compensate for sample stage tilt, drift-corrected and contrast-adjusted by laboratory-built image analysis software in ImageJ and MATLAB (Mathworks). The workflow used to calculate an LAFM map from molecular HS-AFM raw data is outlined in Fig. 3. The key steps in the preparation for the LAFM method are: extraction of molecular observations from images (Fig. 3d, steps 1–5), image expansion (Fig. 3d, step 6; see Methods section 'Image expansion') and creation of a particle gallery with laterally and rotationally well aligned particles (Fig. 3d, steps 7–9). Several image processing packages used for electron microscopy (for example, ref. [52]) allow particle extraction and alignment, and could be used for convenience. The particle gallery of pixel-expanded (0.5 Å per pixel) molecular observations is the entry for the LAFM algorithm, which comprises detection of local maxima, height extraction and merging of height and peaking probabilities (Fig. 3d, steps 10–11; Methods sections 'Detection of local maxima', 'Detection probability', 'Height extraction' and 'Merging height and detection probability') in the final LAFM map. The LAFM method is available as code in the form of an appendix and as an ImageJ plugin (Supplementary Information).

LAFM simulations

2D and 3D LAFM simulations were performed using MATLAB. In 2D simulations (x, z), various model surfaces were created with different features depending on the simulation (Fig. 1b; simulation parameters: tip radius, 20 pixels; feature height, 3 pixels; feature width and separation, 2 pixels; scanning noise, 0.05 (standard deviation, σ), feature fluctuation, 0.3 (σ); the Gaussian surface topography (bottom row) has $\sigma = 20$; varying parameters are used in Extended Data Figs. 2, 3, given in the figure captions). Each topographic feature was given a height higher than the surrounding baseline surface (set at zero). Normally distributed random numbers with set standard deviation were then generated and added to each x position containing a topographic feature, increasing or decreasing the height. These random fluctuations were added independently of neighbouring x positions. A semicircular tip of defined radius was calculated numerically and then scanned across the simulated 2D surface to create a tip-convoluted topography. To simulate the AFM instrument noise, normally distributed random noise was then added in the z direction to the tip-convoluted topography at all positions. Many randomly generated topographies were then analysed using the LAFM algorithm to produce peaking probability and peaking height traces. 3D simulations were run using a similar methodology, however a hemispherical tip was scanned across 3D model surfaces (Extended Data Figs. 4, 5, Supplementary Video 2).

Simulation data are compared to a theoretical resolution limit (Extended Data Fig. 3) on the basis of geometric considerations, assuming a rigid pair of spikes separated by a distance (d) and a height difference (Δh), contacted by a tip radius (R) without noise or fluctuations.

The resolution limit is defined as being resolved if the probe is able to reach a minimum (Δz) below the height of the smallest spike[53]:

$$d = \sqrt{2R}\ (\sqrt{\Delta z} + \sqrt{\Delta z + \Delta h}).$$

The absolute resolution limit under these considerations occurs when maxima can be detected at both spikes when $\Delta z = 0$.

MD simulations of CLC

Construct for MD simulations. The molecular model of the CLC-ec1 dimer used in all MD simulations described in this work was based on the X-ray structure PDB 1OTS[31]. The protonation states of the titratable residues at pH 7 were determined from constant-pH calculations with the neMD/MC (non-equilibrium MD/Monte Carlo) approach[54]. The spatial arrangement of the CLC-ec1 dimer in the bilayer was optimized using the Orientations of Proteins in Membranes (OPM) database[55] and input to the Membrane Builder module on the CHARMM-GUI web server[56] to assemble the protein–membrane system. The CLC-ec1 dimer was embedded in a 629-lipid membrane bilayer containing a ~70:30 mixture of POPE (1-palmitoyl-2-oleoyl-sn-glycero-3-phosphoethanolamine) and POPG (1-palmitoyl-2-oleoyl-sn-glycero-3-phospho-(1'-rac-glycerol)), solvated in 150 mM KCl explicit water to achieve electroneutrality.

MD simulation procedures. The assembled molecular system was subjected to an initial equilibration phase using NAMD[57] (version 2.13) following two protocols. The first used the standard six-step equilibration protocol provided by CHARMM-GUI. The other used a laboratory-built multi-step equilibration, in which the backbone of the protein was first fixed[58]. Backbone constraints were gradually released in three 300-ps steps of force constant change (1 to 0.5 and to 0.1 kcal per mol^{-1} Å^{-2}). The final structures from the equilibration phases were subjected to short (46 ns and 48 ns) unbiased MD with NAMD (2-fs time steps, vdwForceSwitching option, and PME for electrostatic interactions)[59]. The runs were in the NPT ensemble under semi-isotropic pressure coupling at 24 °C. The Nose–Hoover–Langevin piston algorithm[60] was used to control the target P = 1 atm pressure with LangevinPistonPeriod = 50 fs and LangevinPistonDecay = 25 fs. Van der Waals interactions had a cut-off distance of 12 Å. The first phase of production runs (Production 1) was initiated by all-atom velocity resetting and continued with simulations of the system in 50 independent replicates of ~150 ns each (that is, 100 replicates overall for a cumulative 15 µs) using ACEMD[61]. At the conclusion of Production 1, the trajectories were analysed to assess the stability of the bound Cl^- ions, and replicates with the most stably bound Cl^- ions were identified. The final snapshots from 48 replicates were selected as starting points for the next phase, Production 2, in which the systems were simulated using NAMD with the parameters described above for ~120 ns (cumulative 5.76 µs). Run parameters: timestep 4 fs, vdwforceswitching on, switching on, switchdist 7.5, cutoff 9, fullelectfrequency 2, langevindamping 0.1, pme on, and pmegridspacing 1.0. All the simulations used the latest CHARMM36 force-field parameters for proteins, lipids and ions.

Population density maps from the MD trajectories. To analyse the height of protein atoms with respect to the membrane plane during the MD simulations, the symmetry axis of the CLC-ec1 dimer was set perpendicular to the X–Y plane. In analogy to the LAFM method, the highest z-coordinate values on the CLC extracellular surface were selected for each frame to plot the position distribution map. Maps were constructed by taking the 8, 10 and 16 highest points in each frame, leading to the conclusion that detection of more than 8 points resulted in sampling the neighbouring atoms of residues already included in the 8-point set. Thus, the distribution maps were obtained by pooling the 8 highest-z-coordinate peaks from each frame. Analysis performed separately on Production 1 and Production 2 trajectories did not show notable differences, and in the main text we show the results from the analysis of 5.6 µs with 20-ps time strides of Production 2 trajectories. Because both protomers of CLC-ec1 were considered identical, we symmetrized the data by aligning trajectories of each protomer onto another one.

MD simulation of annexin-V P13W-G14W

MD simulations of the mutant annexin-V-P13W-G14W were conducted with Gromacs2019.1[62], using the Amber03 force field[63]. The initial molecular model of annexin-V-P13W-G14W was generated using the X-ray structure PDB 1HVD, and the double mutation introduced using the program Coot[64]. This model was then solvated with ~40,000 water molecules in accordance with the Tip3P water model[65], and neutralized with Na^+ and Cl^- ions to a concentration of 150 mM. The system was placed in a dodecahedron box, with a minimal distance of 1.0 nm between protein and box wall. Van der Waals interactions were implemented with a cutoff at 1.0 nm, and long-range electrostatic effects were treated with the particle mesh Ewald method. The protein–solvent model was then put through four rounds of geometry optimization and energy minimization, followed by a 50-ps protein position-restrained equilibration and an additional 50 ps of unrestrained equilibration. The system was then heated to 300 K using a velocity-rescaling thermostat[66] (50 ps), and equilibrated to a constant pressure of 1 bar using a Parrinello–Rahman barostat (50 ps). Following these equilibration procedures, a time trajectory of 100 ns was simulated at constant temperature and pressure, using time steps of 2 fs and the same thermostat and barostat. The data were then symmetrized along the threefold axis by aligning trajectories of each protomer one onto the other. To build an annexin-V-P13W-G14W mutant structural model that represents the rotamer conformations of the mutated Trp residues, clustering analysis of the simulation trajectories was performed with Gromacs (g_cluster, gromos algorithm)[62], with a root-mean-square deviation cut-off of 0.2 with respect to the mutated Trp residues in positions 13–14. Out of the 10 resulting clusters, the most representative structure was extracted from the centre of the most populated cluster (containing ~50% of total protein structures).

Data availability

The datasets generated and/or analysed during the current study are available from the corresponding author on reasonable request.

Code availability

The custom-written script implemented in ImageJ to create LAFM maps from a stack of aligned and expanded images is available in Supplementary Information. MATLAB codes used in 2D and 3D LAFM simulations are also available in Supplementary Information.

48. Chadda, R. et al. The dimerization equilibrium of a ClC Cl^-/H^+ antiporter in lipid bilayers. *eLife* **5**, e17438 (2016).
49. Burger, W. & Burge, M. J. *Digital Image Processing: An Algorithmic Introduction Using Java* (Springer, 2016).
50. Fukuma, T. & Garcia, R. Atomic- and molecular-resolution mapping of solid–liquid interfaces by 3D atomic force microscopy. *ACS Nano* **12**, 11785–11797 (2018).
51. Lee, B. & Richards, F. M. The interpretation of protein structures: estimation of static accessibility. *J. Mol. Biol.* **55**, 379–400 (1971).
52. Scheres, S. H. W. Semi-automated selection of cryo-EM particles in RELION-1.3. *J. Struct. Biol.* **189**, 114–122 (2015).
53. Bustamante, C. & Keller, D. Scanning force microscopy in biology. *Phys. Today* **48**, 32–38 (1995).
54. Olsson, M. H. M., Sondergaard, C. R., Rostkowski, M. & Jensen, J. H. PROPKA3: consistent treatment of internal and surface residues in empirical pKa predictions. *J. Chem. Theory Comput.* **7**, 525–537 (2011).
55. Lomize, M. A., Lomize, A. L., Pogozheva, I. D. & Mosberg, H. I. OPM: orientations of proteins in membranes database. *Bioinformatics* **22**, 623–625 (2006).
56. Jo, S., Lim, J. B., Klauda, J. B. & Im, W. CHARMM-GUI membrane builder for mixed bilayers and its application to yeast membranes. *Biophys. J.* **97**, 50–58 (2009).
57. Phillips, J. C. et al. Scalable molecular dynamics with NAMD. *J. Comput. Chem.* **26**, 1781–1802 (2005).
58. Khelashvili, G. et al. Spontaneous inward opening of the dopamine transporter is triggered by pip-regulated dynamics of the N-terminus. *ACS Chem. Neurosci.* **6**, 1825–1837 (2015).

59. Essmann, U. et al. A smooth particle mesh Ewald method. *J. Chem. Phys.* **103**, 8577–8593 (1995).
60. Evans, D. J. & Holian, B. L. The Nose–Hoover thermostat. *J. Chem. Phys.* **83**, 4069–4074 (1985).
61. Harvey, M., Giupponi, G. & De Fabritiis, G. ACEMD: accelerated molecular dynamics simulations in the microseconds timescale. *J. Chem. Theory Comput.* **5**, 1632–1639 (2009).
62. Van Der Spoel, D. et al. GROMACS: fast, flexible, and free. *J. Comput. Chem.* **26**, 1701–1718 (2005).
63. Duan, Y. et al. A point-charge force field for molecular mechanics simulations of proteins based on condensed-phase quantum mechanical calculations. *J. Comput. Chem.* **24**, 1999–2012 (2003).
64. Emsley, P. & Cowtan, K. Coot: model-building tools for molecular graphics. *Acta Crystallogr. D* **60**, 2126–2132 (2004).
65. Jorgensen, W. L., Chandrasekhar, J., Madura, J. D., Impey, R. W. & Klein, M. L. Comparison of simple potential functions for simulating liquid water. *J. Chem. Phys.* **79**, 926–935 (1983).
66. Bussi, G., Donadio, D. & Parrinello, M. Canonical sampling through velocity rescaling. *J. Chem. Phys.* **126**, 014101 (2007).

Acknowledgements This work was supported by grants from the National Institute of Health, NIH, DP1AT010874 (to S.S.) and R01GM120260 (to J.L.R.). We thank A. Razavi for help with the initial stages of the MD simulation analysis and for discussions. The computational work was performed using resources of the Oak Ridge Leadership Computing Facility (allocation BIP109 and Director's Discretionary) at the Oak Ridge National Laboratory, which is a DOE Office of Science User Facility supported under contract DE-AC05-00OR22725; resources and support provided at the RPI Artificial Intelligence Multiprocessing Optimized System (AiMOS) system, accessed through an award from the COVID-19 HPC Consortium (https://covid19-hpc-consortium.org/); and the computational resources of the David A. Cofrin Center for Biomedical Information in Institute for Computational Biomedicine at Weill Cornell Medical College. Support from the 1923 Fund is gratefully acknowledged.

Author contributions G.R.H. and S.S. designed the study and developed the LAFM algorithm; J.L.R. purified and reconstituted the CLC-ec1. G.R.H. and S.L. performed HS-AFM experiments. E.K. and G.K. performed CLC MD simulations. S.L. performed A5 P13W-G14W cloning, expression, purification and MD simulations. G.R.H., E.K., G.K., H.W. and S.S. analysed the data. G.R.H., E.K., J.L.R, G.K., H.W. and S.S. wrote the paper.

Competing interests The authors declare no competing interests.

Additional information
Supplementary information The online version contains supplementary material available at https://doi.org/10.1038/s41586-021-03551-x.
Correspondence and requests for materials should be addressed to S.S.
Peer review information *Nature* thanks Franz J. Giessibl, Victor Shahin and the other, anonymous, reviewer(s) for their contribution to the peer review of this work.
Reprints and permissions information is available at http://www.nature.com/reprints.

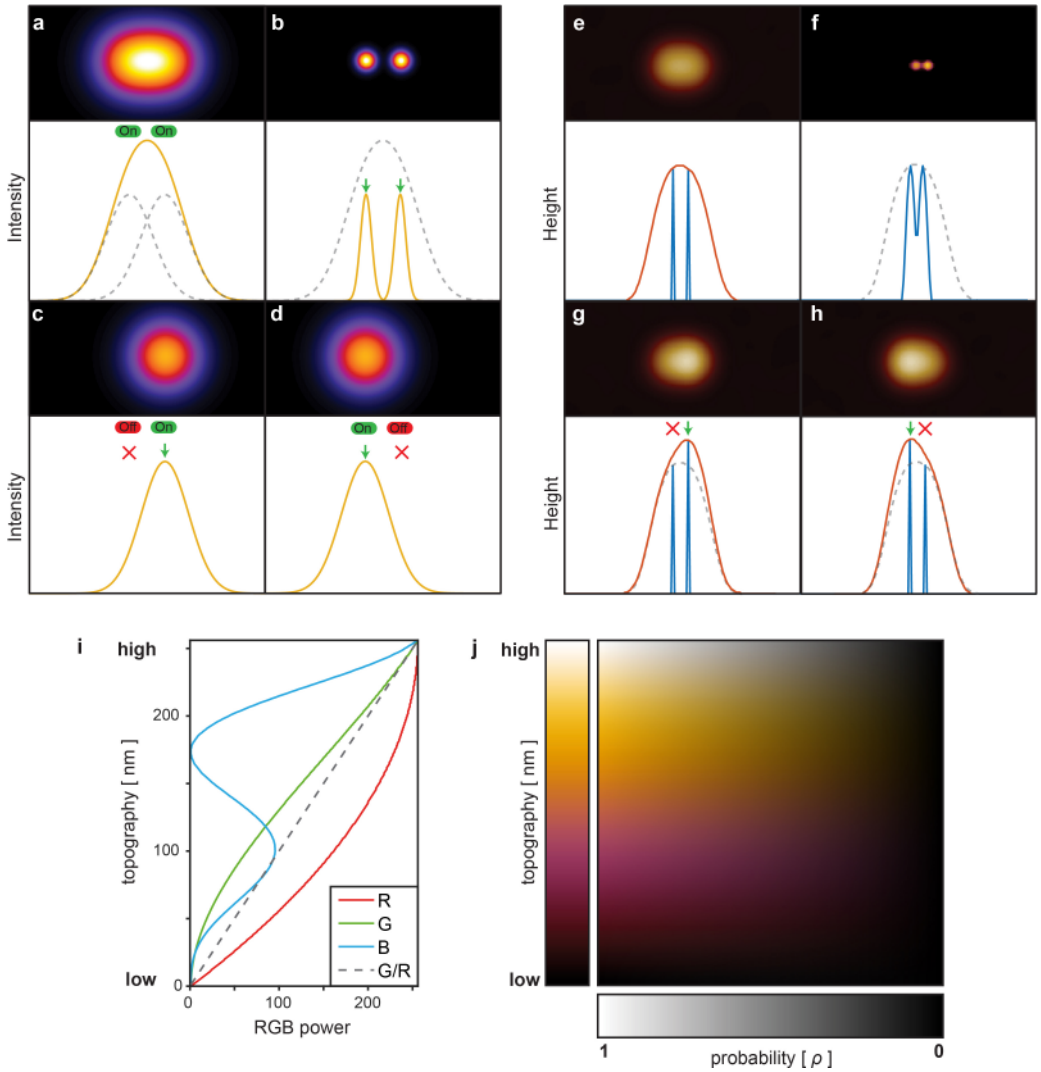

Extended Data Fig. 1 | Localization principles in PALM and LAFM. **a**, A diffraction-limited image/profile of two fluorescent molecules located at a separation distance smaller than the diffraction limit. **b**–**d**, Spatially resolved positions of the fluorophores after application of optical localization methods such as PALM or STORM. The position of each fluorophore can be spatially localized with high precision if the emitted signal can be isolated from neighbouring fluorophores, permitted by stochastic activation of the right (**c**) or left (**d**) fluorophore. **e**, A tip-convoluted AFM image of two structural features located at a separation distance smaller than the sharpness of the AFM tip. **f**–**h**, Spatially resolved positions of structural features after application of LAFM. Stochastic height fluctuations allow the position of each feature to be localized by the protruding height signal of the right (**g**) or left (**h**) feature peaking over the neighbouring features. In **a**–**h**, top panels show 2D intensity/topography images and bottom panels show intensity/height profiles across the central x line of the top panels. **i**, **j**, LAFM false-colour scale used to encode topography and localization peaking probability information. **i**, The LAFM map is encoded by a false-colour scale in which red (R), green (G) and blue (B) values follow the relations: $R(h) = -h^2/255 + 2h - 2$; $G(h) = Rh/255$; $B(h) = h\{\sin[0.036(h + 127)] + 1\}/2$, where h is the topography scale and RGB values range between 0 and 255 (minimum to maximum). The ratio of green to red (G/R) increases linearly with height (dashed line), whereas the blue value increases and oscillates to produce a visually informative false-colour scale. **j**, To incorporate the probability, each picked location is given a Gaussian probability density function that peaks at value 1. To generate the final LAFM map, the peaks of all molecules are merged, and thus an average topography height and related peaking probability (grey scale; bottom) at any location is calculated, resulting in a 2D false-colour table in which each pixel carries the full information about topography and the likeliness of a topography to be detected at this location.

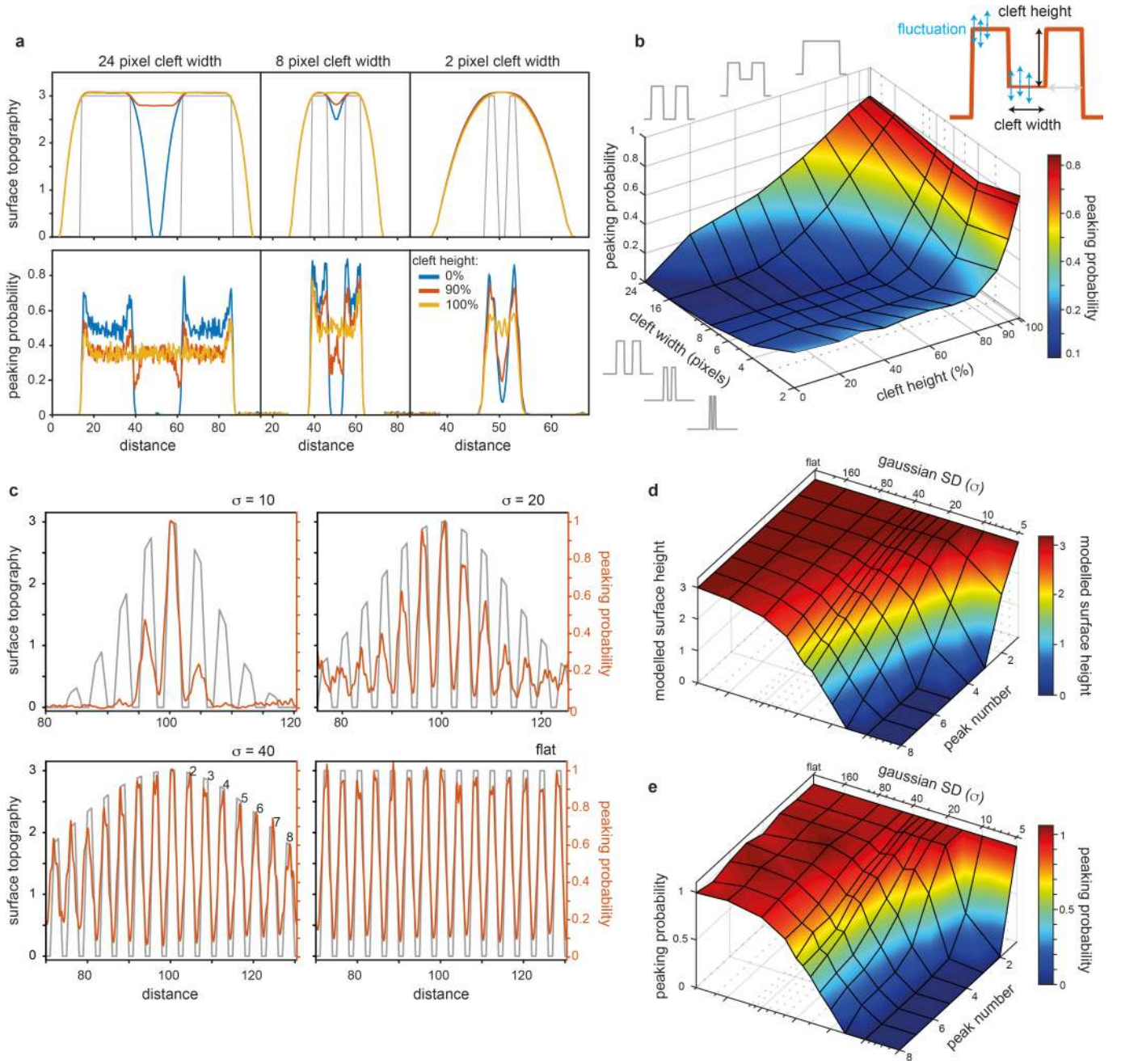

Extended Data Fig. 2 | Simulations of varying cleft height and cleft width, and detection of features in varying topographic superstructures by the LAFM algorithm. a, Example average surface topography (top) and peaking probability (bottom) for 24, 8 and 2 pixels cleft width and cleft heights of 0, 90 and 100%. At a separation of 2 pixels (cleft width), averaging is unable to detect any topography change as the cleft height is changed, because the tip never probes into the cleft. In contrast, the LAFM method reports lower peaking probabilities in this region separating the two features. The detection probability in the cleft areas depends on the tip radius, feature separation and height fluctuation, and is therefore not linear. The height detection in the cleft areas is the same as the topography (see Fig. 1b). **b**, Surface plot showing the peaking probability in the cleft region relative to the pillar positions for varying cleft heights and widths. In the simulations the tip radius is 20 pixels and each surface feature pixel has feature fluctuation standard deviation of 0.3, and fluctuations are independent of neighbouring pixels. **c**, Peak detection of surface features on Gaussian curved surfaces. Features are 2 pixels wide interspersed by 2 pixels multiplied by Gaussian functions with σ = 10, 20, 40 and a flat surface, respectively, scanned by a tip with a radius of 20 pixels (noise, 0.3). **d**, **e**, Surface plots of the height of the model surface (**d**) and the relative peaking probability compared to the probability at the central peak (**e**) for each Gaussian surface topography up to a distance of 8 peaks from the central peak. The probability of peak detection is affected by neighbouring peaks and tip radius, leading to a correct representation of the height, but a nonlinear relation between surface height and peaking probability. There is little to no lateral error of localization position detection on peaks of different local height.

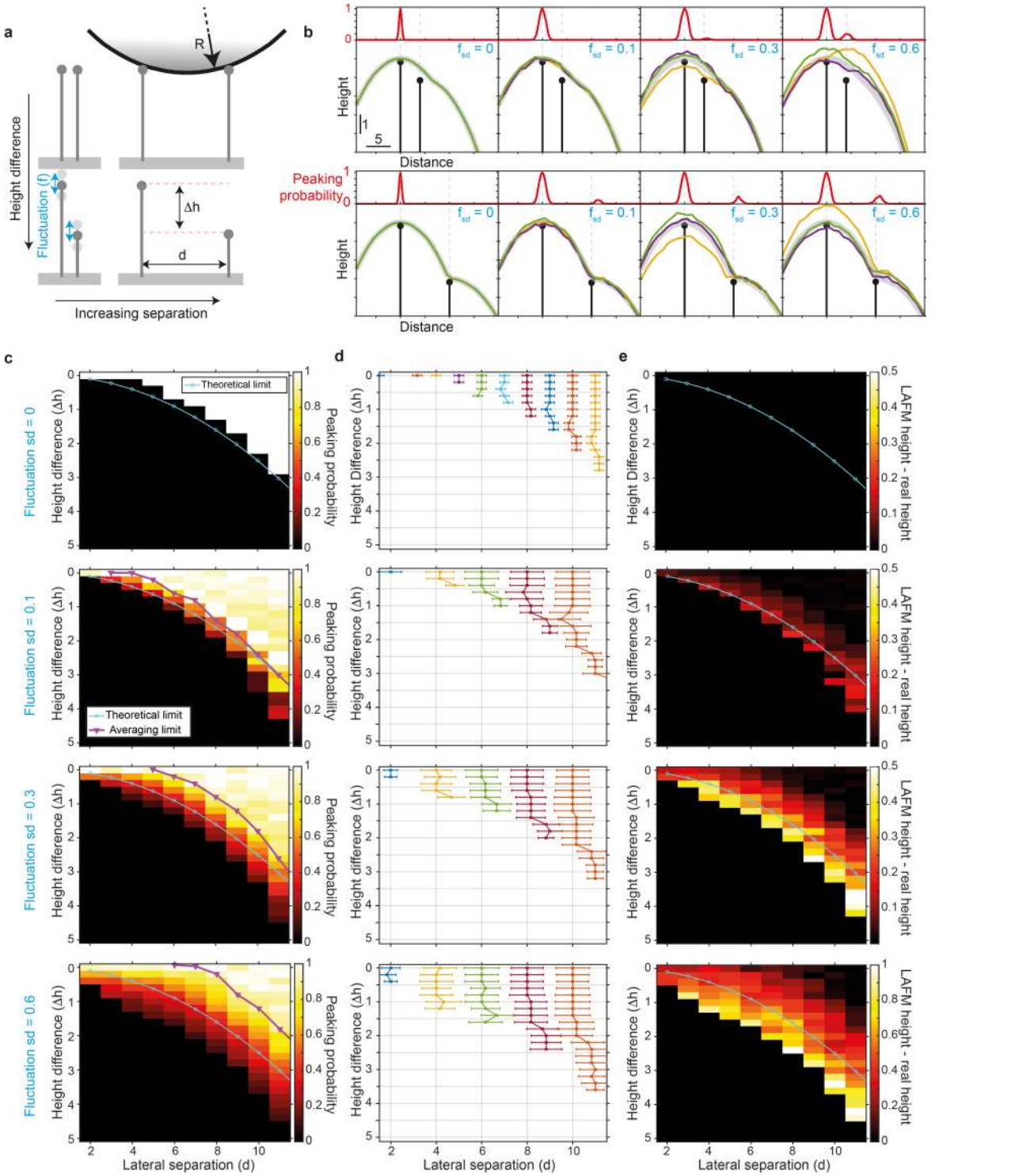

Extended Data Fig. 3 | Simulations of feature detection with varying topographic height by the LAFM algorithm. a, Schematic of two sharp features in which the feature separation, d, and height difference, Δh, are varied by changing the position/height of the secondary feature. Feature fluctuations are then simulated by adding or subtracting a randomly generated height (normally distributed), f, with a set standard deviation, f_{sd}, before being scanned by a model AFM tip of radius R. **b**, Example simulations of topographies with $d = 4$, $\Delta h = 1$ (top) and $d = 10$, $\Delta h = 3$ (bottom), scanned by a tip with a radius $R = 20$, for varying amounts of feature fluctuation from left to right ($f_{sd} = 0$, 0.1, 0.3 and 0.6). Coloured lines are three representative simulated topography traces and thick grey lines show the average scanned topography ($n = 2{,}000$). Panels above each topography plot give the LAFM peaking probability at each position in the topography. **c**, Matrix of simulations plotted as an image in which each pixel represents the LAFM peaking probability of the secondary feature for a different height difference–separation distance combination. The black pixels indicate zero probability and therefore no peak detection. Also plotted are the theoretical resolution limits according to geometrical arguments allowing the apex of the tip to contact the feature (see Methods section 'LAFM simulations') and the average AFM maximum resolution, according to whether a local maximum can be detected for the secondary feature in the average topography. **d**, Lateral position of peaking probability for the different height difference–separation distance combinations. Each coloured line represents a different lateral separation and error bars show the peak width (±s.d.). **e**, Matrix of simulations plotted as an image in which each pixel represents the difference between the detected LAFM average height and the model height for each height difference–separation distance combination. In **c**–**e**, each row from top to bottom represents a different feature fluctuation standard deviation of 0, 0.1, 0.3 and 0.6. For each fluctuation level, 286 Δh–d combinations were each simulated 2,000 times.

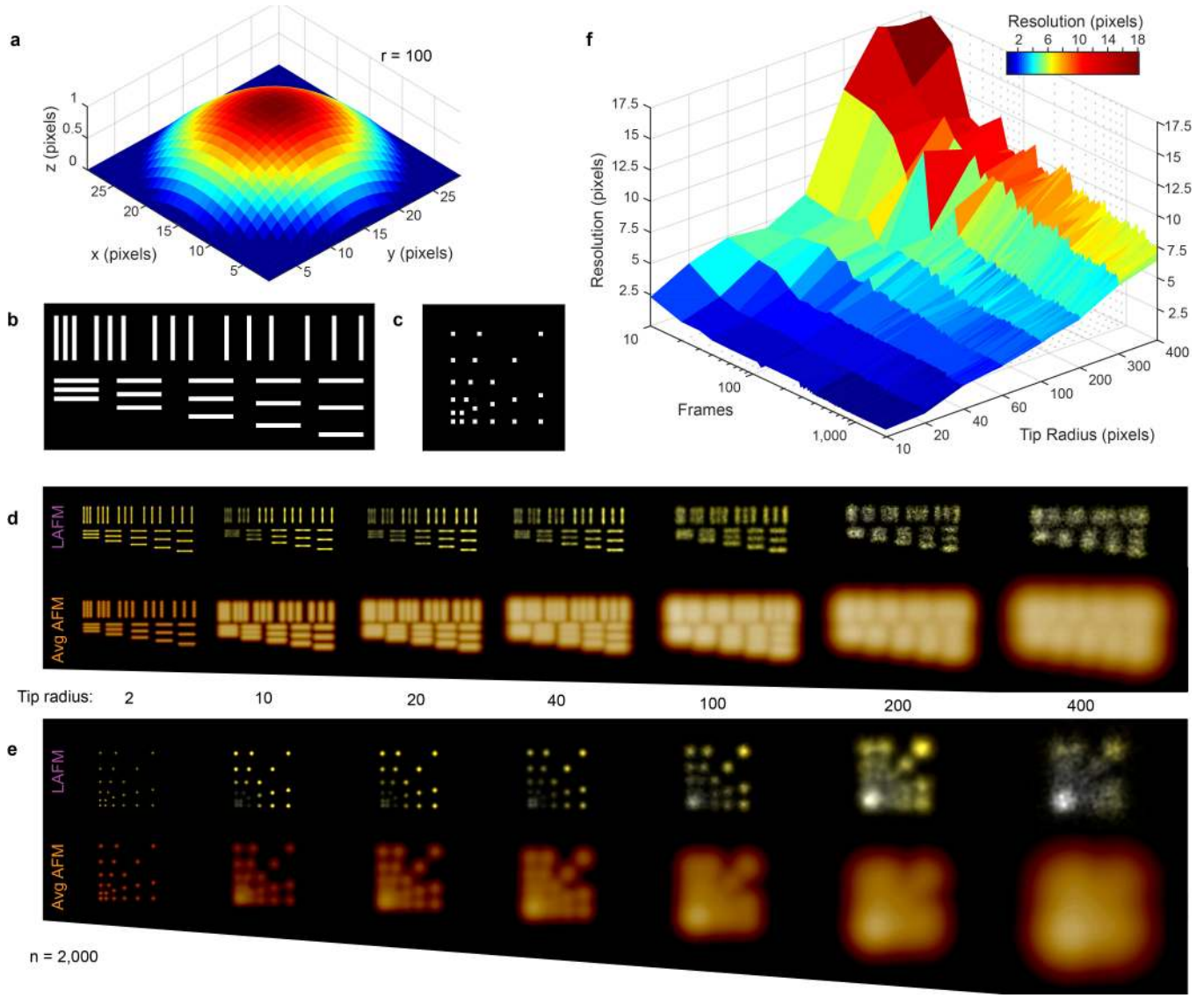

Extended Data Fig. 4 | Simulations to assess the ability to resolve two spatial features in LAFM maps. a–**e**, A tip with varying tip radius *r* (here 100 pixels) is scanned over two different simulation surfaces featuring topographic lines (**b**) or topographic points (**c**). These lines and points have a size of 1 pixel in the *x*, *y* and *z* directions, and are interspaced by 1, 2, 3, 4 and 5 pixels. This procedure, including sample fluctuations and contouring noise, results in individual simulated topography images for the line topography (**d**) and the point topography (**e**) that are either averaged or analysed using the LAFM algorithm (average AFM and LAFM maps result from merging 2,000 simulated topographies). **f**, Surface plot of the simulated LAFM map resolution determined by FRC as a function of the number of merged images and simulation tip radius, showing that when ~100 particles are analysed, features of size ~1/40 (for a blunt tip) to ~1/5 (for a sharp tip) of the tip radius can be resolved.

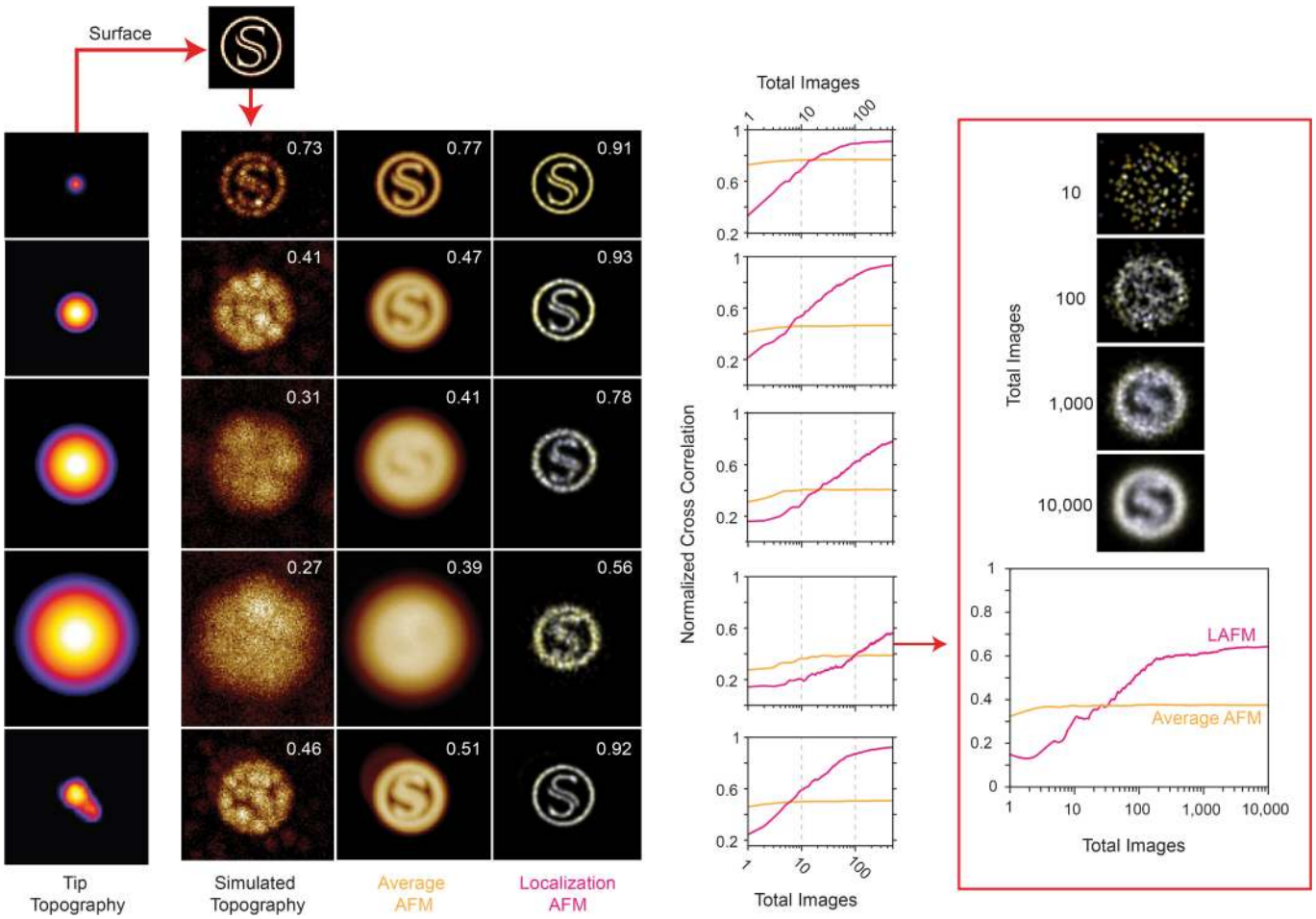

Extended Data Fig. 5 | Influence of tip radius and number of merged particles for the calculation of LAFM maps. First column: simulation experiments in which the surface topography (S) with a ring diameter of 35 pixels (top) is probed by five different tips, four spherical tips with increasing radius (1–4, $R = 10, 100, 300, 600$) and an irregular tip with a 'double-tip' protrusion ($R = 40$, peak to peak = 12 pixels). Second column: simulated individual raw data images (comprising random noise) of the topography (S) contoured by the various tips. Third column: average image of 500 simulated images. Fourth column: LAFM map derived from the same 500 simulated images. The numbers in the top right corner of each image are the normalized cross-correlation values (CCV [0,1]) between the image and the surface model. The graphs show the dependence of the CCV between average or LAFM maps with the topography as a function of the number of merged particles. In the case of the sharpest tip (top row), the LAFM map CCV plateaus after merging ~50 molecules. Right: analysis of localization map image quality and CCV for the largest tip (4) when merging up to 10,000 particles. In the case of the bluntest tip, the LAFM map CCV plateaus after merging ~500 particles.

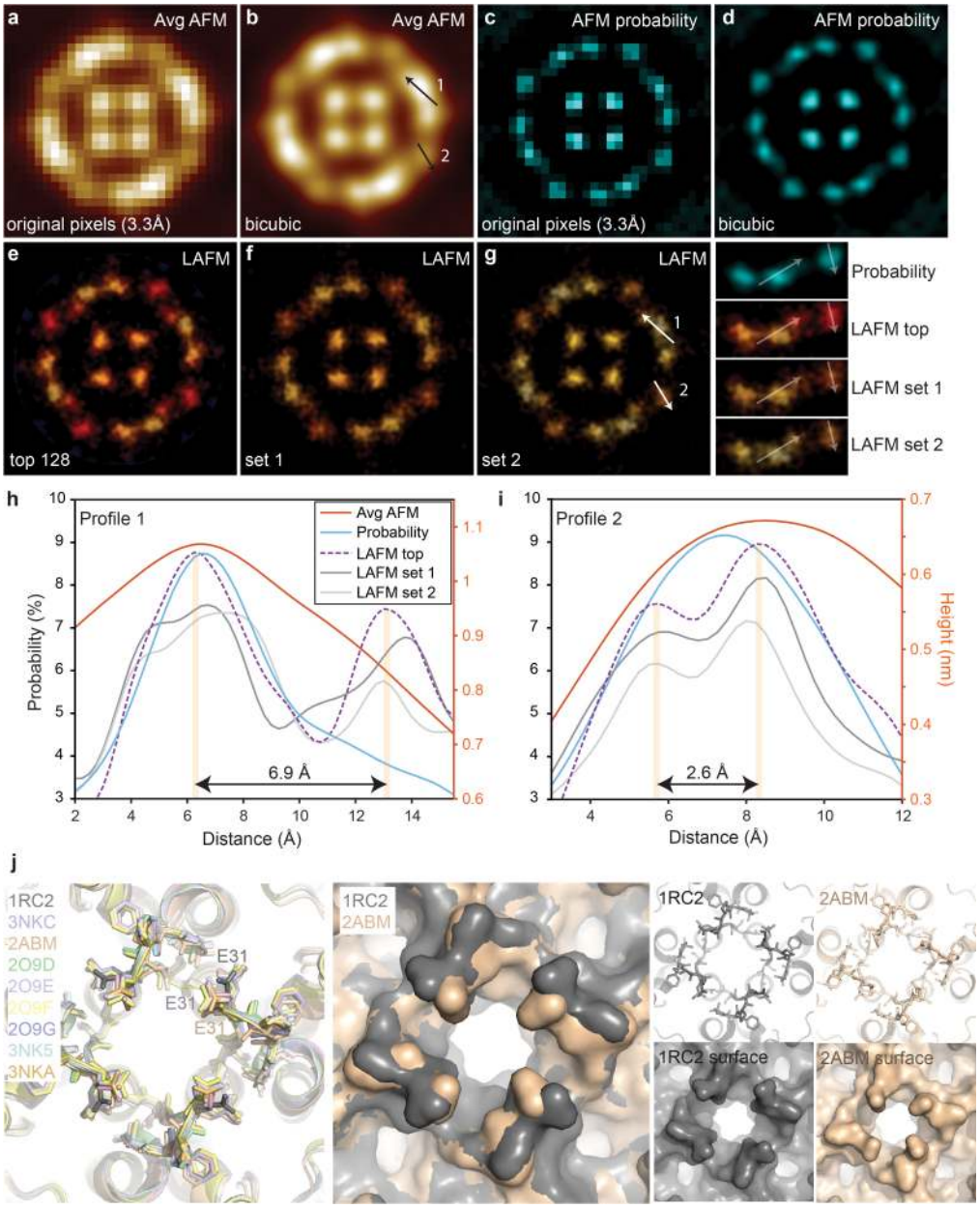

Extended Data Fig. 6 | Resolution comparison between averaging, peak probability and LAFM methods applied to AFM images of AqpZ. **a**, **b**, Average AFM images at the original pixel sampling of 3.3 Å per pixel (**a**) and after bicubic interpolation to 0.5 Å per pixel (**b**). **c**, **d**, Peak probability maps[20] calculated at the original pixel sampling of 3.3 Å per pixel (**c**) and after bicubic interpolation to 0.5 Å per pixel (**d**) (n = 128 for average height and probability maps). **e**–**g**, LAFM probability maps calculated at 0.5 Å per pixel with 1.4-Å Gaussian peaking probability distribution using 128 AqpZ particles with highest correlation to the average map (**e**) or using two randomly generated independent 128-particle sets from a set of 256 to create two independent half-maps (**f**, **g**). **h**, **i**, Line profiles along arrow 1 (**h**) and arrow 2 (**i**) in **b** and **g**, measuring height (for average AFM images) and probability across structural features in the average AFM, probability and LAFM probability maps. The features in the two line profiles are consistently resolved near and below the highest theoretical resolution based on the discrete sampling of a single image (raw data Nyquist frequency is 1/(6.6 Å)). **j**, Left: alignment of the nine available AqpZ X-ray structures. The structures can be grouped with respect to the side-chain orientation of E31 in the a-loop. Middle: surface representation overlay of 1RC2 and 2ABM, highlighting how the different E31 rotamers alter the surface structure. Right: representative structures (top) and surface representations (bottom) of 1RC2 and 2ABM. The 2ABM structure features an E31 conformation that fits closely the reconstructed LAFM map (**g** and Fig. 2a, b), suggesting that in the membrane, physiological buffer and room-temperature E31 is in a conformation similar to the 2ABM structure.

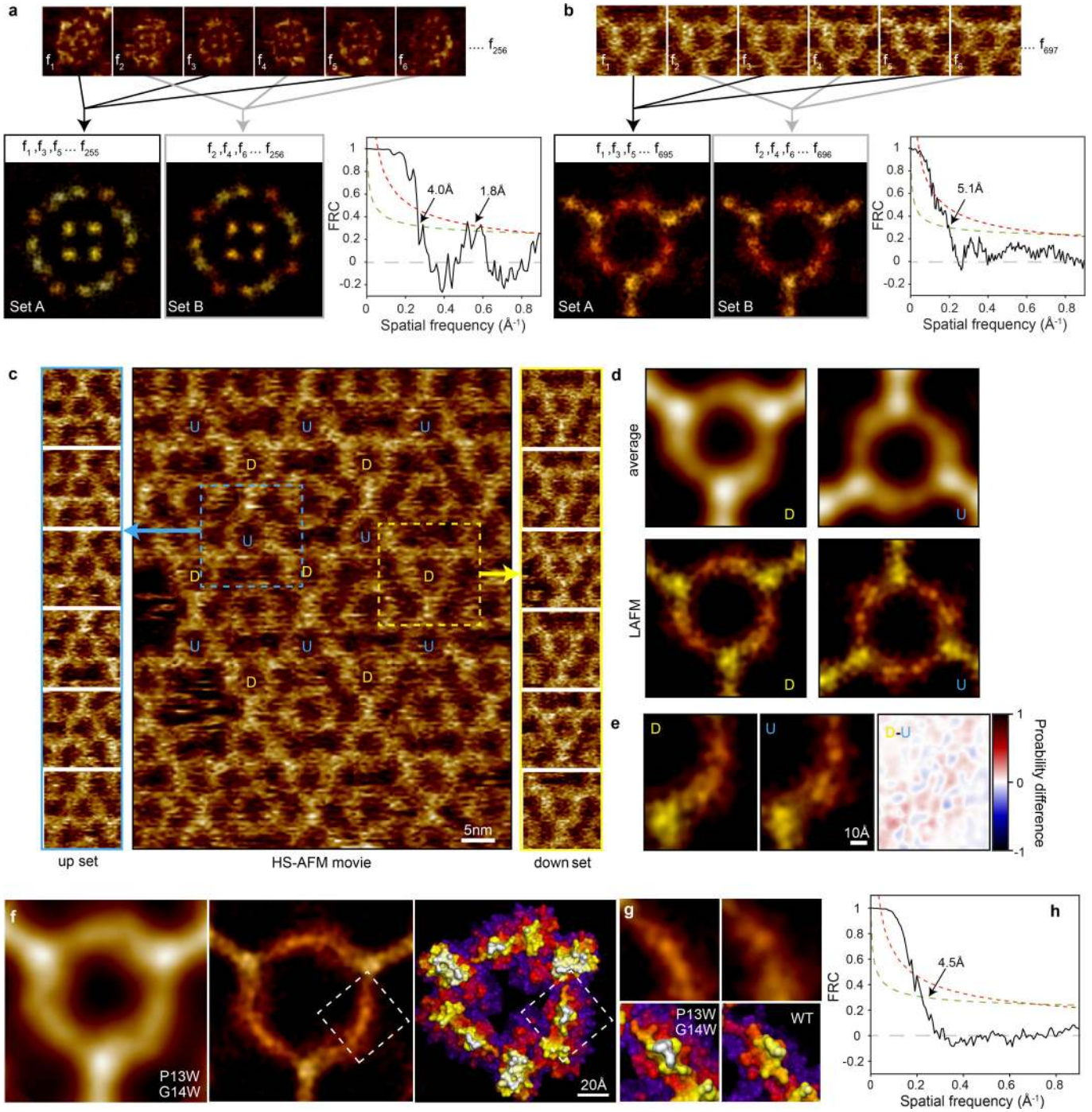

Extended Data Fig. 7 | LAFM map resolution and quality assessment. **a**, **b**, AFM image frames of AqpZ (**a**) and A5 (**b**) are alternately extracted into two separate image sets (Set A and Set B). The LAFM algorithm is then applied to each image set to produce two independent LAFM half-maps of AqpZ (left) and A5 (right). FRC analysis of the LAFM half-maps is then used for quantification of the power as a function of the spatial resolution in the AqpZ dataset (left) and A5 (right). Dashed and dotted lines show the 1/2-bit and 3σ criteria, respectively. **c**, Image from an HS-AFM video of A5 in a *p*6 lattice (centre), showing that the A5 lattice contains trimers of two fixed orientations labelled U and D. The two A5 trimer types U and D are scanned with different relative orientation with respect to the HS-AFM fast-scan axis. Extracted images of the trimers in each of the two orientations are shown on either side for set U (up; left) and set D (down; right). **d**, Average AFM and LAFM maps filtered to 5 Å of A5 trimers in the U (n = 700) and D (n = 697) orientations. **e**, Structural comparison between LAFM maps obtained from the independent differently orientated A5 and the probability difference map (image U has been rotated 180° to allow direct comparison). **f**, Analysis of A5 P13W-G14W mutant (data acquisition: A5 P13W-G14W on a DOPC/DOPS (1/1) bilayer imaged by HS-AFM in amplitude modulation mode; scan speed, 1 frame per second; scan area, 120 nm; image size, 300 pixels; pixel sampling, 4.0 Å per pixel). Average AFM map (left), LAFM map (middle; pixel sampling, 0.5 Å per pixel; number of particles n = 300, filtered to 4.5 Å) and surface representations of an A5 P13W-G14W structural model. **g**, Detail views of the LAFM maps (top) and structures (bottom; MD-refined structural model of A5 P13W-G14W and X-ray structure of A5). The mutations appear to induce conformational rearrangements in the N-terminal region (residues 1 to 15), with an increased height and peaking probability at positions 13–14 in the LAFM map. **h**, FRC analysis of the A5 P13W-G14W LAFM map.

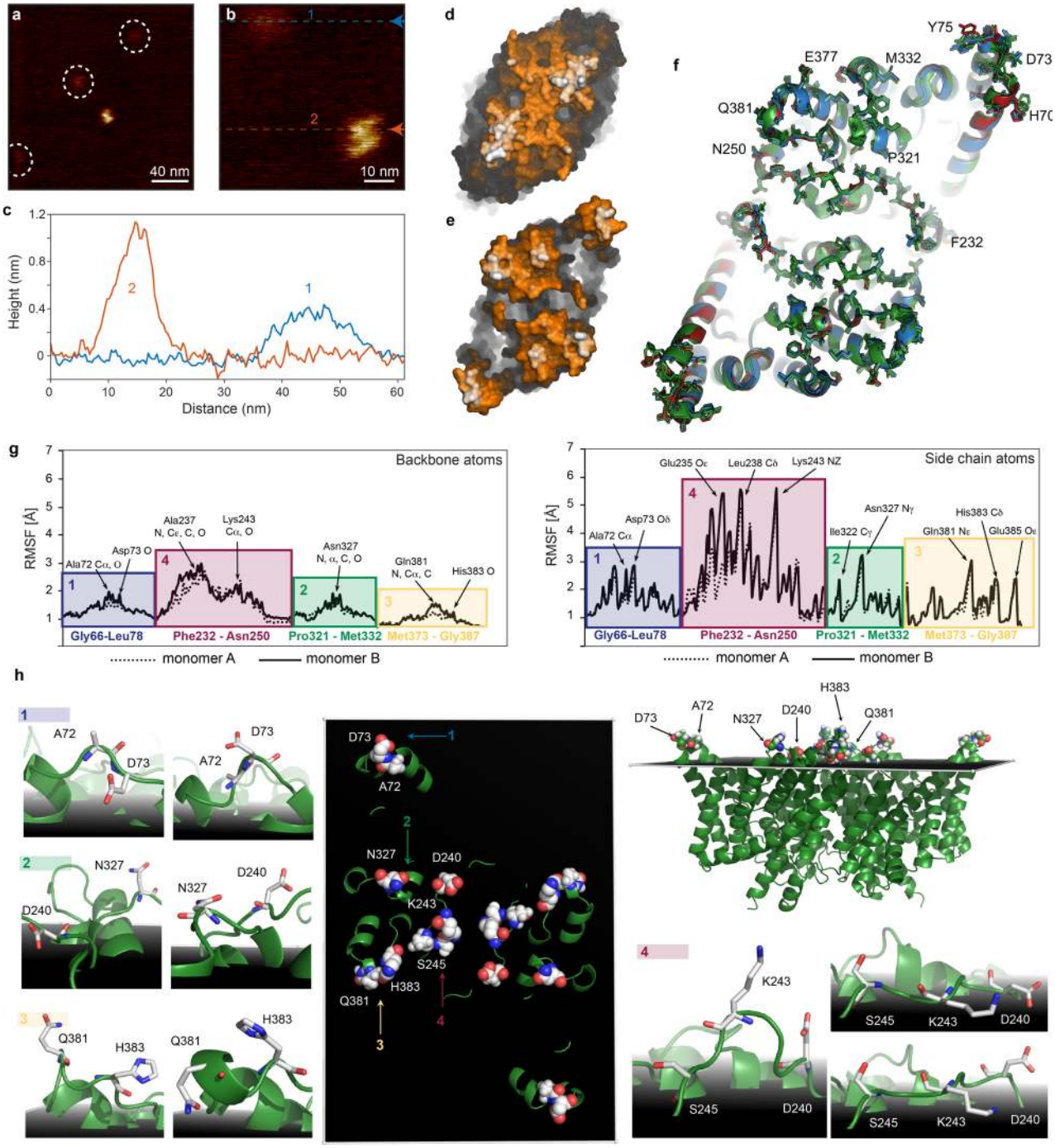

Extended Data Fig. 8 | Extracellular sidedness assignment of CLC-ec1. **a**, **b**, HS-AFM video frames of CLC-ec1 in a POPE:POPG (ratio of 2:1 w-w) bilayer: molecules protruding just a little and S-shaped molecules protruding farther from the membrane were detected. **c**, Section analysis of the two molecules shown in **b**: one molecular species protrudes only ~4 Å from the bilayer, whereas the S-shaped representation of the CLC-ec1 protrudes ~11 Å from the membrane surface. **d**, **e**, Surface representations of the intracellular (**d**) and extracellular (**e**) faces of the X-ray structure (PDB 1OTS). Based on the structural comparison, we assigned the S-shaped CLC-ec1 HS-AFM topography to the extracellular face. Only the S-shaped extracellular-face molecules were integrated into the LAFM analysis. **f**, Alignment of CLC-ec1 X-ray structures (PDB: 1OTS, 2FEE, 2H2P, 3DET, 2HTK, 4KKB) exhibiting essentially identical conformations, leading to the suggestion that the transport mechanism implicates only minor side-chain motion. NMR, computational and biochemical studies have suggested larger-scale movements of helices N[39], O[38] and B[37] in transport. Protruding residues detectable by LAFM are shown in sticks and are labelled. **g**, Root-mean-square fluctuations (RMSF) of the backbone (left) and the side-chain (right) atoms of membrane-protruding extracellular CLC-ec1 residues from the analysis of MD trajectories at pH 7. The coloured blocks demarcate the groups of residues attributed to the four major LAFM and MD population map peaks, and the key residues are labelled. **h**, Key residues contributing to the peak observations in LAFM maps in the PDB 1OTS structure (middle and top right panels). The black shadowed plane illustrates the average position of the lipid phosphate atoms throughout the MD trajectories and thus represents the membrane level. Surrounding images (labelled 1 to 4) show representative snapshots from MD simulations highlighting re-orientations/fluctuations of the side chains of the residues contributing to the LAFM-detected peaks.

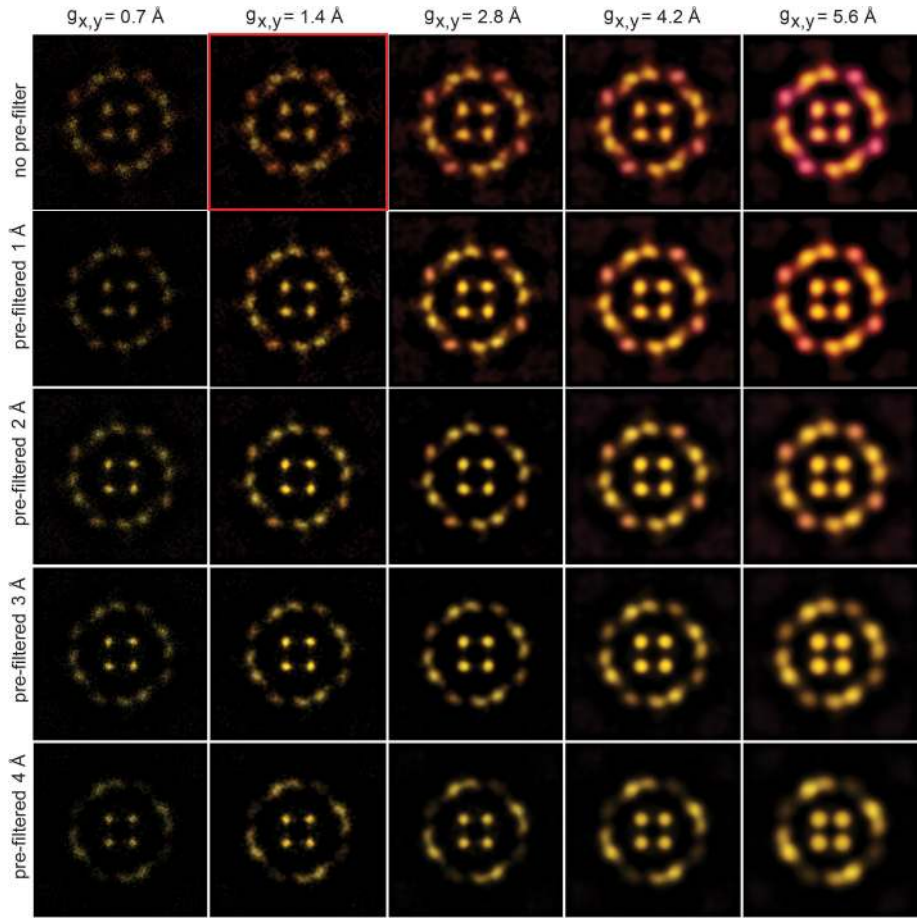

Extended Data Fig. 9 | Analysis of the influence of the 2D Gaussian radius to the peaking events and data pre-filtering on LAFM map reconstruction. Horizontal panels show reconstructed AqpZ LAFM maps of peaking detections with varying 2D Gaussian radii of 0.7 Å, 1.4 Å, 2.8 Å, 4.2 Å and 5.6 Å (without any pre-processing Gaussian filtering). The vertical panels show reconstructed AqpZ LAFM maps of images pre-processed with varying Gaussian filters of 0 Å, 1 Å, 2 Å, 3 Å and 4 Å while varying the peaking detection 2D Gaussian radius. The comparison shows that applying a filter to the data before applying the LAFM method results in a loss of information, particularly from features that are smaller or of lower height. Whereas increasing the 2D Gaussian radius applied to each localization during the LAFM method results in a loss of lateral resolution in the reconstructed LAFM map. Highlighted in red is our standard method for constructing LAFM maps, using no pre-filtering and a peaking detection 2D Gaussian of 1.4 Å, approximating the solvent-accessible surface of atoms.

Extended Data Table 1 | Set of available PDB structures of CLC-ec1 at various conditions

PDB ID	pH	Mutations	Ions	BB RMSD (Å)
1OTS	9.5		NaCl	reference
1KPK	8.5		Na_2SO_4 / Li_2SO_4	0.785
1KPL*	4.6	M26L/C264V	Na_2SO_4 / Li_2SO_4	1.169
1OTT	9.5	E148A	NaCl	0.465
1OTU	9.5	E148Q	NaCl	0.589
2EXY	8.5	E148Q	TART	0.646
2EZ0	9.5	S107A/E148Q/Y445A	NaBr	0.722
2FEC	7.5	E203Q	NaBr	0.425
2FED	7.5	E203Q	NaCl	0.427
2FEE	7.5		NaBr	0.362
2H2P	7.5		KSCN	0.515
2H2S	7.5	E148A	KSeCN	0.491
2HLF	9.5	Y445E	NaBr	0.378
2HT2	8.5	Y445H	TART	0.654
2HT3	7.5	Y445L	TART	0.581
2HT4	8.0	Y445W	NaBr	0.533
2HTK	8.5	Y445A	TART	0.378
2R9H	9.5	Q207C	NaCl / TART	0.558
3DET	5.5	E148A / Y445A	KCl	0.415
3EJY	9.5		NaBr	0.425
3EJZ	8.5	E203V	NaBr	0.426
3NMO†	9.5		$LiNO_3$	0.565
4ENE	8.5		$CaCl_2$	0.442
4FTP	9.5	E202Y		0.877
4KJP	9.5			0.412
4KK5	9.0		NaF / NaBr	0.282
4KK8	8.5	E148Q	NaF	0.422
4KKB	7.0	E148A	NaF / NaBr	0.454
4KKC	9.0	E148A	NaBr	0.679
5HD8	9.0	D417C	TART	0.597

The root-mean-square deviation (RMSD) values are calculated for backbone atoms with respect to the PDB 1OTS structure as reference. All CLC X-ray structures exhibited essentially identical conformations.

*A low-pH structure of CLC from *Salmonella typhimurium*.

†Structure of monomer.